We are IntechOpen, the world's leading publisher of Open Access books Built by scientists, for scientists

4,800
Open access books available

122,000
International authors and editors

135M
Downloads

Our authors are among the

154
Countries delivered to

TOP 1%
most cited scientists

12.2%
Contributors from top 500 universities

CLARIVATE ANALYTICS
BOOK CITATION INDEX
INDEXED

WEB OF SCIENCE™

Selection of our books indexed in the Book Citation Index
in Web of Science™ Core Collection (BKCI)

Interested in publishing with us?
Contact book.department@intechopen.com

Numbers displayed above are based on latest data collected.
For more information visit www.intechopen.com

Mechanical fault detection in induction motor drives through stator current monitoring - Theory and application examples

Martin Blödt
Siemens AG
Germany

Pierre Granjon and Bertrand Raison
Grenoble-INP
France

Jérémi Regnier
INP Toulouse
France

1. Introduction

1.1 General Introduction

In a wide variety of industrial applications, an increasing demand exists to improve the reliability and availability of electrical systems. Popular examples include systems in aircraft, electric railway traction, power plant cooling or industrial production lines. A sudden failure of a system in these examples may lead to cost expensive downtime, damage to surrounding equipment or even danger to humans. Monitoring and failure detection improve the reliability and availability of an existing system. Since various failures degrade relatively slowly, there is a potential for fault detection followed by corrective maintenance at an early stage. This avoids the sudden, total system failure which can have serious consequences.

Electric machines are a key element in many electrical systems. Amongst all types of electric motors, induction motors are a frequent example due to their simplicity of construction, robustness and high efficiency. Common failures occurring in electrical drives can be roughly classified into:

Electrical faults: stator winding short circuit, broken rotor bar, broken end-ring, inverter failure

Mechanical faults: rotor eccentricity, bearing faults, shaft misalignment, load faults (unbalance, gearbox fault or general failure in the load part of the drive)

A reliability survey on large electric motors (>200 HP) revealed that most failures are due to bearing ($\approx 44\%$) and winding faults ($\approx 26\%$) (IEEE motor reliability working group (1985a))

(Engelmann & Middendorf (1995)). Similar results were obtained in an EPRI (Electric Power Research Institute) sponsored survey (Albrecht et al. (1987)). These studies concerned only the electric motor and not the whole drive including the load, but they show that mechanical fault detection is of great concern in electric drives.

A growing number of induction motors operates in variable speed drives. In this case, the motor is not directly connected to the power grid but supplied by an inverter. The inverter provides voltage of variable amplitude and frequency in order to vary the mechanical speed. Hence, this work addresses the problem of condition monitoring of mechanical faults in variable speed induction motor drives. A signal based approach is chosen i.e. the fault detection and diagnosis are only based on processing and analysis of measured signals and not on real-time models.

1.2 Motor Current Signature Analysis

A common approach for monitoring mechanical failures is vibration monitoring. Due to the nature of mechanical faults, their effect is most straightforward on the vibrations of the affected component. Since vibrations lead to acoustic noise, noise monitoring is also a possible approach. However, these methods are expensive since they require costly additional transducers. Their use only makes sense in case of large machines or highly critical applications. A cost effective alternative is stator current based monitoring since a current measurement is easy to implement. Moreover, current measurements are already available in many drives for control or protection purposes. However, the effects of mechanical failures on the motor stator current are complex to analyze. Therefore, stator current based monitoring is undoubtedly more difficult than vibration monitoring.

Another advantage of current based monitoring over vibration analysis is the limited number of necessary sensors. An electrical drive can be a complex and extended mechanical system. For complete monitoring, a large number of vibration transducers must be placed on the different system components that are likely to fail e.g. bearings, gearboxes, stator frame, load. However, a severe mechanical problem in any component influences necessarily the electric machine through load torque and shaft speed. This signifies that the motor can be considered as a type of intermediate transducer where various fault effects converge together. This strongly limits the number of necessary sensors. However, since numerous fault effects come together, fault diagnosis and discrimination become more difficult or sometimes even impossible.

A literature survey showed a lack of analytical models that account for the mechanical fault effect on the stator current. Most authors simply give expressions of additional frequencies but no precise stator current signal model. In various works, numerical machine models accounting for the fault are used. However, they do not provide analytical stator current expressions which are important for the choice of suitable signal analysis and detection strategies.

The most widely used method for stator current processing in this context is spectrum estimation. In general, the stator current power spectral density is estimated using Fourier transform based techniques such as the periodogram. These methods require stationary signals i.e. they are inappropriate when frequencies vary with respect to time such as during speed transients. Advanced methods for non-stationary signal analysis are required.

The organization of the present work is the following. Section 2 analyses the effects of load torque oscillations and dynamic eccentricity on the stator current. In section 3, suitable signal processing methods for stator current analysis are introduced. Experimental results under laboratory conditions are presented in section 4. Section 5 examines the detection of misalign-

Mechanical fault detection in induction motor drives through stator
current monitoring - Theory and application examples
453

ment faults in electric winches including analysis of experimental data from a real winch. Bearing faults are investigated apart in section 6 from a theoretical and practical point of view since they can introduce particular eccentricities and load torque oscillations.

2. Theoretical study of mechanical fault effects on stator current

The key assumption for the development of the theoretical models is that mechanical faults mainly produce two effects on induction machines: additional load torque oscillations at characteristic frequencies and/or airgap eccentricity.
Load torque oscillations can be caused by the following faults:

- load unbalance (not necessarily a fault but can also be inherent to the load type)

- shaft misalignment

- gearbox fault e.g. broken tooth

- bearing faults

Airgap eccentricity i.e. a non-uniform airgap can be for example the consequence of bearing wear or bearing failure, bad motor assembly with rotor unbalance or a rotor which is not perfectly centered. In general, eccentricity will be a sign for a mechanical problem within the electric motor whereas load torque oscillations point to a fault that is located outside of the motor.
The method used to study the influence of the periodic load torque variation and the rotor eccentricity on the stator current is the magnetomotive force (MMF) and permeance wave approach (Yang (1981)) (Timár (1989)) (Heller & Hamata (1977)). This approach is traditionally used for the calculation of the magnetic airgap field with respect to rotor and stator slotting or static and dynamic eccentricity (Cameron & Thomson (1986)) (Dorrell et al. (1997)).
First, the rotor and stator MMF are calculated which are directly related to the current flowing in the windings. The second important quantity is the airgap permeance Λ which is directly proportional to the inverse of the airgap length g. The magnetic field in the airgap can then be determined by multiplying the permeance by the sum of rotor and stator MMFs. The equivalent magnetic flux in one phase is obtained by integration of the magnetic field in each turn of the phase winding. The induced phase voltage, related to the current by the stator voltage equation, is then deduced from the magnetic flux.
As this work also considers variable speed drives, the supply frequency f_s and the characteristic fault frequency f_c may vary. Note that f_c can be for example the time-varying rotational frequency f_r. The theoretical stator current analysis during transients, however, is identical to the steady state if relatively slow frequency variations of f_s and f_c are considered.

2.1 Load torque oscillations

The influence of load torque oscillations on the stator current has been published for a general case by the authors in (Blödt, Chabert, Regnier & Faucher (2006)) (Blödt (2006)). The development will be shortly resumed in the following.

2.1.1 Effect on Rotor and Stator MMF

Under a mechanical fault, the load torque as a function of time is modeled by a constant component Γ_{const} and an additional component varying at the characteristic frequency f_c, depending on the fault type. It can be for example the rotational frequency f_r with load unbalance or a particular gearbox frequency in case of a gearbox fault. The first term of the variable

component Fourier series is a cosine with frequency f_c. For the sake of clarity and since they are usually of smaller amplitude, higher order terms at kf_c are neglected in the following and only the fundamental term is considered. The load torque can therefore be described by:

$$\Gamma_{load}(t) = \Gamma_{const} + \Gamma_c \cos(\omega_c t) \tag{1}$$

where Γ_c is the amplitude of the load torque oscillation and $\omega_c = 2\pi f_c$.

The machine mechanical equation relates the torque oscillation to the motor speed ω_r and to the mechanical rotor position θ_r as follows:

$$\sum \Gamma(t) = \Gamma_{motor} - \Gamma_{load}(t) = J\frac{d\omega_r}{dt} = J\frac{d^2\theta_r}{dt^2} \tag{2}$$

where Γ_{motor} is the constant electromagnetic torque produced by the machine, J is the total inertia of the machine and the load.

After integrating twice, $\theta_r(t)$ is obtained as:

$$\theta_r(t) = \int_{t_0}^{t} \omega_r(\tau) d\tau = \frac{\Gamma_c}{J\omega_c^2} \cos(\omega_c t) + \omega_{r0}t \tag{3}$$

where ω_{r0} is the constant part of the motor speed. This equation shows that in contrast to the healthy machine where $\theta_r(t) = \omega_{r0}t$, oscillations at the characteristic frequencies are present on the mechanical rotor position.

The oscillations of the mechanical rotor position θ_r act on the rotor MMF. In a healthy state without faults, the fundamental rotor MMF in the rotor reference frame (R) is a wave with p pole pairs and frequency sf_s, given by:

$$F_r^{(R)}(\theta', t) = F_r \cos(p\theta' - s\omega_s t) \tag{4}$$

where θ' is the mechanical angle in the rotor reference frame (R) and s is the motor slip. Higher order space and time harmonics are neglected.
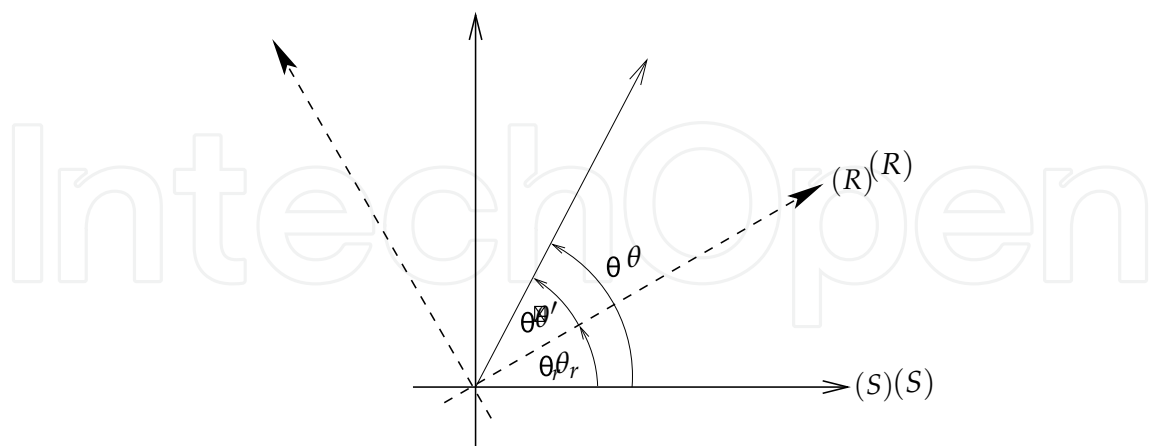

Fig. 1. Stator (S) and rotor (R) reference frame

Figure 1 illustrates the transformation between the rotor and stator reference frame, defined by $\theta = \theta' + \theta_r$. Using (3), this leads to:

$$\theta' = \theta - \omega_{r0}t - \frac{\Gamma_c}{J\omega_c^2} \cos(\omega_c t) \tag{5}$$

Thus, the rotor MMF given in (4) can be transformed to the stationary stator reference frame using (5) and the relation $\omega_{r0} = \omega_s(1-s)/p$:

$$F_r(\theta,t) = F_r \cos\left(p\theta - \omega_s t - \beta\cos\left(\omega_c t\right)\right) \tag{6}$$

with:

$$\beta = p\frac{\Gamma_c}{J\omega_c^2} \tag{7}$$

Equation (6) clearly shows that the load torque oscillations at frequency f_c lead to a phase modulation of the rotor MMF in the stator reference frame. This phase modulation is characterized by the introduction of the term $\beta\cos(\omega_c t)$ in the phase of the MMF wave. The parameter β is generally called the modulation index. For physically reasonable values J, Γ_c and ω_c, the approximation $\beta \ll 1$ holds in most cases.

The fault has no direct effect on the stator MMF and so it is considered to have the following form:

$$F_s(\theta,t) = F_s \cos\left(p\theta - \omega_s t - \varphi_s\right) \tag{8}$$

φ_s is the initial phase difference between rotor and stator MMF. As in the case of the rotor MMF, only the fundamental space and time harmonic is taken into account; higher order space and time harmonics are neglected.

2.1.2 Effect on Flux Density and Stator Current

The airgap flux density $B(\theta,t)$ is the product of total MMF and airgap permeance Λ. The airgap permeance is supposed to be constant because slotting effects and eccentricity are not taken into account for the sake of clarity and simplicity.

$$\begin{aligned}
B(\theta,t) &= [F_s(\theta,t) + F_r(\theta,t)]\,\Lambda \\
&= B_s\cos\left(p\theta - \omega_s t - \varphi_s\right) \\
&\quad + B_r\cos\left(p\theta - \omega_s t - \beta\cos\left(\omega_c t\right)\right)
\end{aligned} \tag{9}$$

The phase modulation of the flux density $B(\theta,t)$ exists for the flux $\Phi(t)$ itself, as $\Phi(t)$ is obtained by simple integration of $B(\theta,t)$ with respect to the winding structure. The winding structure has only an influence on the amplitudes of the flux harmonic components, not on their frequencies. Therefore, $\Phi(t)$ in an arbitrary phase can be expressed in a general form:

$$\Phi(t) = \Phi_s\cos\left(\omega_s t + \varphi_s\right) + \Phi_r\cos\left(\omega_s t + \beta\cos\left(\omega_c t\right)\right) \tag{10}$$

The relation between the flux and the stator current in a considered phase is given by the stator voltage equation:

$$V(t) = R_s I(t) + \frac{d\Phi(t)}{dt} \tag{11}$$

With $V(t)$ imposed by the voltage source, the resulting stator current will be in a linear relation to the time derivative of the phase flux $\Phi(t)$ and will have an equivalent frequency content. Differentiating (10) leads to:

$$\begin{aligned}
\frac{d}{dt}\Phi(t) = &-\omega_s\Phi_s\sin\left(\omega_s t + \varphi_s\right) \\
&-\omega_s\Phi_r\sin\left(\omega_s t + \beta\cos\left(\omega_c t\right)\right) \\
&+\omega_c\beta\Phi_r\sin\left(\omega_s t + \beta\cos\left(\omega_c t\right)\right)\sin(\omega_c t)
\end{aligned} \tag{12}$$

The amplitude of the last term is smaller than that of the other terms because $\beta \ll 1$. Thus, the last term in (12) will be neglected in the following.

As a consequence, the stator current in an arbitrary phase can be expressed in a general form:

$$
\begin{aligned}
I_{to}(t) &= i_{st}(t) + i_{rt}(t) \\
&= I_{st} \sin(\omega_s t + \varphi_s) + I_{rt} \sin(\omega_s t + \beta \cos(\omega_c t))
\end{aligned}
\tag{13}
$$

Therefore the stator current $I(t)$ can be considered as the sum of two components. The term $i_{st}(t)$ results from the stator MMF and it is not modulated. The term $i_{rt}(t)$, which is a direct consequence of the rotor MMF shows the phase modulation due to the considered load torque oscillations. The healthy case is obtained for $\beta = 0$.

In this study, the time harmonics of rotor MMF and the non-uniform airgap permeance have not been considered. However, the harmonics of supply frequency f_s and the rotor slot harmonics will theoretically show the same phase modulation as the fundamental component.

2.2 Airgap Eccentricity

Airgap eccentricity leads to an airgap length that is no longer constant with respect to the stator circumference angle θ and/or time. In general, three types of airgap eccentricity can be distinguished (see Fig. 2):

Static eccentricity: The rotor geometrical and rotational centers are identical, but different from the stator center. The point of minimal airgap length is stationary with respect to the stator.

Dynamic eccentricity: The rotor geometrical center differs from the rotational center. The rotational center is identical with the stator geometrical center. The point of minimal airgap length is moving with respect to the stator.

Mixed eccentricity: The two effects are combined. The rotor geometrical and rotational center as well as the stator geometrical center are different.

In the following theoretical development, static and dynamic eccentricity will be considered.
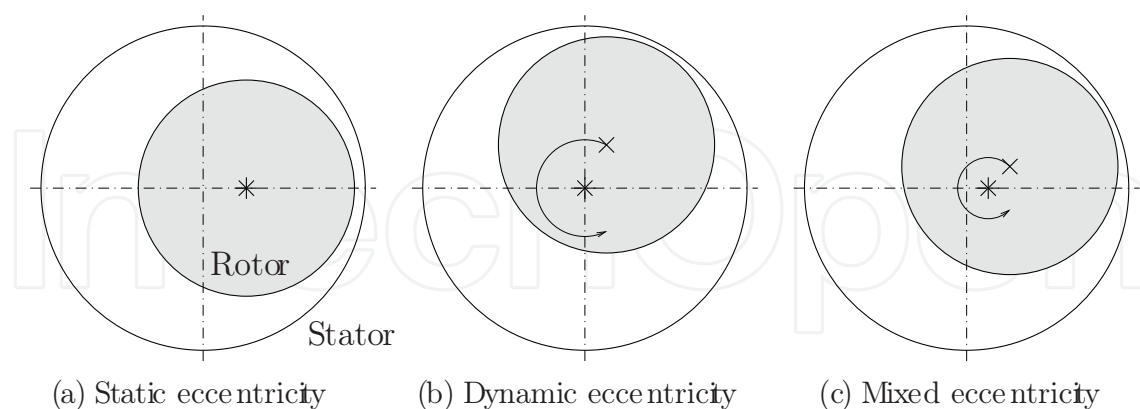

(a) Static eccentricity   (b) Dynamic eccentricity   (c) Mixed eccentricity

Fig. 2. Schematic representation of static, dynamic and mixed eccentricity. $\times$ denotes the rotor geometrical center, $*$ the rotor rotational center

The airgap length $g(\theta, t)$ can be approximated for a small airgap and low levels of static or dynamic eccentricity by the following expression (Dorrell et al. (1997)):

$$
\begin{aligned}
g_{se}(\theta, t) &\approx g_0(1 - \delta_s \cos(\theta)) \\
g_{de}(\theta, t) &\approx g_0(1 - \delta_d \cos(\theta - \omega_r t))
\end{aligned}
\tag{14}
$$

where δ_s, δ_d denote the relative degrees of static or dynamic eccentricity and g_0 the mean airgap length without eccentricity. Note that static eccentricity can be considered as a special case of dynamic eccentricity since $g_{se}(\theta,t)$ corresponds to $g_{de}(\theta,t)$ with $\omega_r = 0$, i.e. the point of minimum airgap length is stationary. Since dynamic eccentricity is more general, it will mainly be considered in the following.

The airgap permeance $\Lambda(\theta,t)$ is obtained as the inverse of $g(\theta,t)$ multiplied by the permeability of free space μ_0. Following a classical approach, the permeance is written as a Fourier series (Cameron & Thomson (1986)):

$$\Lambda_{de}(\theta,t) = \Lambda_0 + \sum_{i_{ecc}=1}^{\infty} \Lambda_{i_{ecc}} \cos(i_{ecc}\theta - i_{ecc}\omega_r t) \tag{15}$$

where $\Lambda_0 = \mu_0/g_0$ is the permeance without eccentricity. The higher order coefficients of the Fourier series can be written as (Cameron & Thomson (1986)):

$$\Lambda_{i_{ecc}} = \frac{2\mu_0(1 - \sqrt{1-\delta^2})^{i_{ecc}}}{g_0 \delta_d^{i_{ecc}} \sqrt{1-\delta^2}} \tag{16}$$

Dorrell has shown in (Dorrell (1996)) that the coefficients with $i_{ecc} \geq 2$ are rather small for $\delta_d < 40\%$. For the sake of simplicity, they are neglected in the following considerations.

The airgap flux density is the product of permeance with the magnetomotive force (MMF). The total fundamental MMF wave can be written as:

$$F_{tot}(\theta,t) = F_1 \cos(p\theta - \omega_s t - \varphi_t) \tag{17}$$

with φ_t the initial phase. Hence, the flux density in presence of dynamic eccentricity is:

$$B_{de}(\theta,t) \approx B_1\left[1 + 2\frac{\Lambda_1}{\Lambda_0}\cos(\theta - \omega_r t)\right]\cos(p\theta - \omega_s t - \varphi_t) \tag{18}$$

with $B_1 = \Lambda_0 F_1$

The fraction $2\Lambda_1/\Lambda_0$ equals approximately δ_d for small levels of eccentricity. The airgap flux density can therefore be written as:

$$B_{de}(\theta,t) = B_1\left[1 + \delta_d \cos(\theta - \omega_r t)\right]\cos(p\theta - \omega_s t - \varphi_t) \tag{19}$$

This equation shows the fundamental effect of dynamic eccentricity on the airgap magnetic flux density : the modified airgap permeance causes an amplitude modulation of the fundamental flux density wave with respect to time and space. The AM modulation index is approximately the degree of dynamic eccentricity δ.

In case of static eccentricity, the fundamental flux density expresses as:

$$B_{se}(\theta,t) = B_1\left[1 + \delta_s \cos(\theta)\right]\cos(p\theta - \omega_s t - \varphi_t) \tag{20}$$

which shows that static eccentricity leads only to flux density AM with respect to space. Consequently, the amplitude modulation can also be found on the stator current $I(t)$ (see section 2.1.2) that is expressed as follows in case of dynamic eccentricity:

$$I_{de}(t) = I_1\left[1 + \alpha \cos(\omega_r t)\right]\cos(\omega_s t - \varphi_i) \tag{21}$$

In this expression, I_1 denotes the amplitude of the stator current fundamental component, α the AM modulation index which is proportional to the degree of dynamic eccentricity δ_d. Static eccentricity does not lead to frequencies different from ω_s since the corresponding additional flux density waves are also at the supply pulsation ω_s. It can be concluded that theoretically, pure static eccentricity cannot be detected by stator current analysis.

3. Signal processing tools for fault detection and diagnosis

The previous section has shown that load torque oscillations cause a phase modulation on one stator current component according to (13). On the other hand, dynamic airgap eccentricity leads to amplitude modulation of the stator current (see (21)). In this section, signal processing methods for detection of both modulation types in the stator current will be presented and discussed.

In order to simplify calculations, all signals will be considered in their complex form, the so-called analytical signal (Boashash (2003)) (Flandrin (1999)). The analytical signal $z(t)$ is related to the real signal $x(t)$ via the Hilbert Transform $H\{.\}$:

$$z(t) = x(t) + jH\{x(t)\} \tag{22}$$

The analytical signal contains the same information as the real signal but its Fourier transform is zero at negative frequencies.

3.1 Power Spectral Density
3.1.1 Definition

The classical method for signal analysis in the frequency domain is the estimation of the Power Spectral Density (PSD) based on the discrete Fourier transform of the signal $x[n]$. The PSD indicates the distribution of signal energy with respect to the frequency. The common estimation method for the PSD is the periodogram $P_{xx}(f)$ (Kay (1988)), defined as the square of the N-point Fourier transform divided by N:

$$P_{xx}(f) = \frac{1}{N} \left| \sum_{n=0}^{N-1} x(n) e^{-j2\pi fn} \right|^2 \tag{23}$$

3.1.2 Application

The PSD represents the basic signal analysis tool for stationary signals i.e. it can be used in case of a constant or quasi-constant supply frequency during the observation interval.

The absolute value of the Fourier transform $|I(f)|$ of the stator current PM signal (13) is obtained as follows (see Blödt, Chabert, Regnier & Faucher (2006) for details):

$$|I_{to}(f)| = (I_{st} + I_{rt} J_0(\beta))\, \delta(f - f_s)$$
$$+ I_{rt} \sum_{n=-\infty}^{+\infty} J_n(\beta)\, \delta\big(f - (f_s \pm nf_c)\big) \tag{24}$$

where J_n denotes the n-th order Bessel function of the first kind and $\delta(f)$ is the Dirac delta function. For small modulation index β, the Bessel functions of order $n \geq 2$ are very small and may be neglected (the so-called narrowband approximation). It becomes clear through this expression that the fault leads to sideband components of the fundamental at $f_s \pm nf_c$. When the modulation index β is small, only the first order sidebands at $f_s \pm f_c$ will be visible and their amplitudes will be approximately $J_1(\beta)I_{rt} \approx 0.5\beta I_{rt}$.

The Fourier transform magnitude of the AM stator current signal according to (21) is:

$$|I_{de}(f)| = I_1 \delta(f - f_s) + \frac{1}{2}\alpha I_1 \delta\big(f - (f_s \pm f_c)\big) \tag{25}$$

The amplitude modulation leads to two sideband components at $f_s \pm f_c$ with equal amplitude $\alpha I_1 / 2$. Therefore, the spectral signature of the AM and PM signal is identical if the modulation

frequency is equal and the PM modulation index is small. This can be the case when e.g. load unbalance and dynamic rotor eccentricity are considered as faults.

It can be concluded that the PSD is a simple analysis tool for stationary drive conditions. It is not suitable for analysis when the drive speed is varying. Another drawback is that PM and AM cannot be clearly distinguished.

3.2 Instantaneous Frequency
3.2.1 Definition
For a complex monocomponent signal $z(t) = a(t)e^{j\varphi(t)}$, the instantaneous frequency $f_i(t)$ is defined by (Boashash (2003)):

$$f_i(t) = \frac{1}{2\pi}\frac{d}{dt}\varphi(t) \tag{26}$$

where $\varphi(t)$ is the instantaneous phase and $a(t)$ the instantaneous amplitude of the analytical signal $z(t)$.

3.2.2 Application
The instantaneous frequency (IF) of a monocomponent phase modulated signal can be calculated using the definition (26). For the phase modulated stator current component $i_{rt}(t)$ (see second term of equation (13)), it can be expressed as:

$$f_{i,i_{rt}}(t) = f_s - f_c\beta\sin(\omega_c t) \tag{27}$$

The fault has therefore a direct effect on the IF of the stator current component $i_{rt}(t)$. In the healthy case, its IF is constant; in the faulty case, a time varying component with frequency f_c appears.

If the complex multicomponent PM signal according to (13) is considered, the calculation of its IF leads to the following expression:

$$f_{i,I}(t) = f_s - f_c\beta\sin(\omega_c t)\frac{1}{1 + a(t)} \tag{28}$$

with

$$a(t) = \frac{I_{st}^2 + I_{st}I_{rt}\cos\left(\beta\cos\left(\omega_c t\right) - \varphi_s\right)}{I_{rt}^2 + I_{st}I_{rt}\cos\left(\beta\cos\left(\omega_c t\right) - \varphi_s\right)} \tag{29}$$

Using reasonable approximations, it can be shown that $1/(1 + a(t))$ is composed of a constant component with only small oscillations. Hence, the IF of (13) may be approximated by:

$$f_{i,I}(t) \approx f_s - Cf_c\beta\sin(\omega_c t) \tag{30}$$

where C is a constant, $C < 1$. Numerical evaluations confirm this approximation. It can therefore be concluded, that the multicomponent PM signal IF corresponding to the stator current also shows fault-related oscillations at f_c which may be used for detection.

The IF of an AM stator current signal according to (21) is simply a constant at frequency f_s. In contrast to the PM stator current signal, no time-variable component is present. The AM modulation index α is not reflected in the IF. Consequently, the stator current IF cannot be used for amplitude modulation detection i.e. airgap eccentricity related faults.

3.3 Wigner Distribution

The Wigner Distribution (WD) belongs to the class of time-frequency signal analysis tools. It provides a signal representation with respect to time and frequency which can be interpreted as a distribution of the signal energy.

3.3.1 Definition

The WD is defined as follows (Flandrin (1999)):

$$W_x(t,f) = \int_{-\infty}^{+\infty} x\left(t + \frac{\tau}{2}\right) x^*\left(t - \frac{\tau}{2}\right) e^{-j2\pi f\tau} d\tau \tag{31}$$

This formula can be seen as the Fourier transform of a kernel $K_x(\tau,t)$ with respect to the delay variable τ. The kernel is similar to an autocorrelation function.

An interesting property of the WD is its perfect concentration on the instantaneous frequency in the case of a linear frequency modulation. However, other types of modulations (e.g. in our case sinusoidal phase modulations) produce so-called inner interference terms in the distribution (Mecklenbräuker & Hlawatsch (1997)). Note that the interferences may however be used for detection purposes as it will be shown in the following.

Another important drawback of the distribution is its non-linearity due to the quadratic nature. When the sum of two signals is considered, so-called outer interference terms appear in the distribution at time instants or frequencies where there should not be any signal energy (Mecklenbräuker & Hlawatsch (1997)). The interference terms can be reduced by using e.g. the Pseudo Wigner Distribution which includes an additional smoothing window (see section 3.4).

3.3.2 Application

The stator current in the presence of load torque oscillations can be considered as the sum of a pure frequency and a phase modulated signal (see (13)). The detailed calculations of the stator current WD can be found in (Blödt, Chabert, Regnier & Faucher (2006)). The following approximate expression is obtained for small β:

$$\begin{aligned}
W_{i_{pm}}(t,f) &\approx \left(I_{rt}^2 + I_{st}^2\right) \delta(f - f_s) \\
&\quad - I_{rt}^2 \beta \sin(\omega_c t) \delta(f - f_s - \frac{f_c}{2}) \\
&\quad + I_{rt}^2 \beta \sin(\omega_c t) \delta(f - f_s + \frac{f_c}{2})
\end{aligned} \tag{32}$$

The WD of the PM stator current is therefore a central frequency at f_s with sidebands at $f_s \pm f_c/2$. These components have time-varying amplitudes at frequency f_c. It is important to note that the lower sideband has the opposed sign to the upper sideband for a given point in time i.e. a phase shift of π exists theoretically between the two sidebands.

The WD of the AM signal according to (21) is calculated in details in (Blödt, Regnier & Faucher (2006)). The following approximate expression is obtained for small modulation indices α:

$$W_{i_{am}}(t,f) \approx I_1^2 \delta(f - f_s) + \alpha \cos(\omega_r t) I_1^2 \delta\left(f - f_s \pm \frac{f_r}{2}\right) \tag{33}$$

The AM signature on the WD is therefore sidebands at $f_s \pm f_r/2$. The sidebands oscillate at shaft rotational frequency f_r, their amplitude is αI_1^2. It should be noted that the signature is

similar to the PM signal but with the important difference that the upper and lower sideband oscillations have the same amplitudes for a given point in time i.e. they are in phase.

3.4 Illustration with Synthesized Signals

In order to validate the preceding theoretical considerations, the periodogram and WD of AM and PM signals are calculated numerically with synthesized signals. The signals are discrete versions of the continuous time signals in (13) and (21) with the following parameters: $I_{st} = I_{rt} = \sqrt{2}/2$, $I_1 = \sqrt{2}$, $\alpha = \beta = 0.1$, $\varphi_s = -\pi/8$, $f_s = 0.25$ and $f_c = f_r = 0.125$ normalized frequency. These parameters are coherent with a realistic application, apart from the strong modulation indices which are used for demonstration purposes. White zero-mean Gaussian noise is added with a signal to noise ration of 50 dB. The signal length is $N = 512$ samples.

First, the periodogram of both signals is calculated (see Fig. 3). Both spectra show the fundamental component with sidebands at $f_s \pm f_r$. The higher order sidebands of the PM signal are buried in the noise floor so that both spectral signatures are identical.

(a) PM signal   (b) AM signal
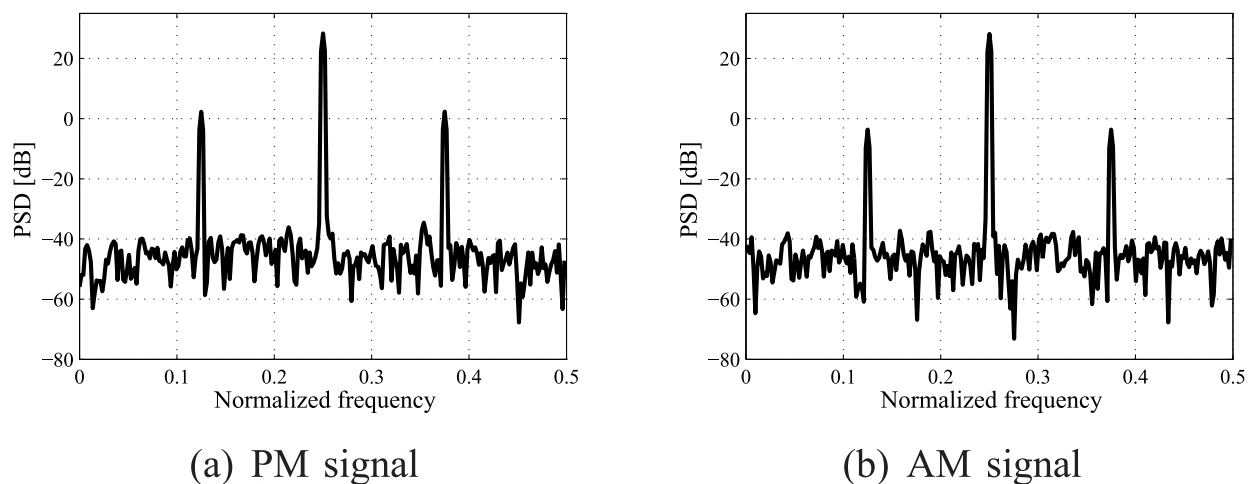
Fig. 3. Power spectral density of synthesized PM and AM signals.

The WD is often replaced in practical applications with the Pseudo Wigner Distribution (PWD). The PWD is a smoothed and windowed version of the WD, defined as follows: (Flandrin (1999)):

$$PW_x(t,f) = \int_{-\infty}^{+\infty} p(\tau) x\left(t + \frac{\tau}{2}\right) x^*\left(t - \frac{\tau}{2}\right) e^{-j2\pi f\tau} d\tau \qquad (34)$$

where $p(\tau)$ is the smoothing window. In the following, a Hanning window of length $N/4$ is used. The time-frequency distributions are calculated using the Matlab$^{\circledR}$ Time-Frequency Toolbox (Auger et al. (1995/1996)). The PWD of the PM and AM stator current signals is displayed in Fig. 4. A constant frequency at $f_s = 0.25$ is visible in each case. Sidebands resulting from modulation appear at $f_s \pm f_r/2$ in both cases. The zoom on the interference structure shows that the sidebands are oscillating at f_r. According to the theory, the sidebands are phase-shifted by approximately π in the PM case whereas they are in phase with the AM signal.

For illustrating the stator current IF analysis, a simulated transient stator current signal is used. The supply frequency $f_s(t)$ varies from 0.05 to 0.25 normalized frequency. The modulation frequency $f_c(t)$ is half the supply frequency. The IF of the transient PM and AM stator

(a) PM signal

(b) AM signal

(c) Zoom on PM signal
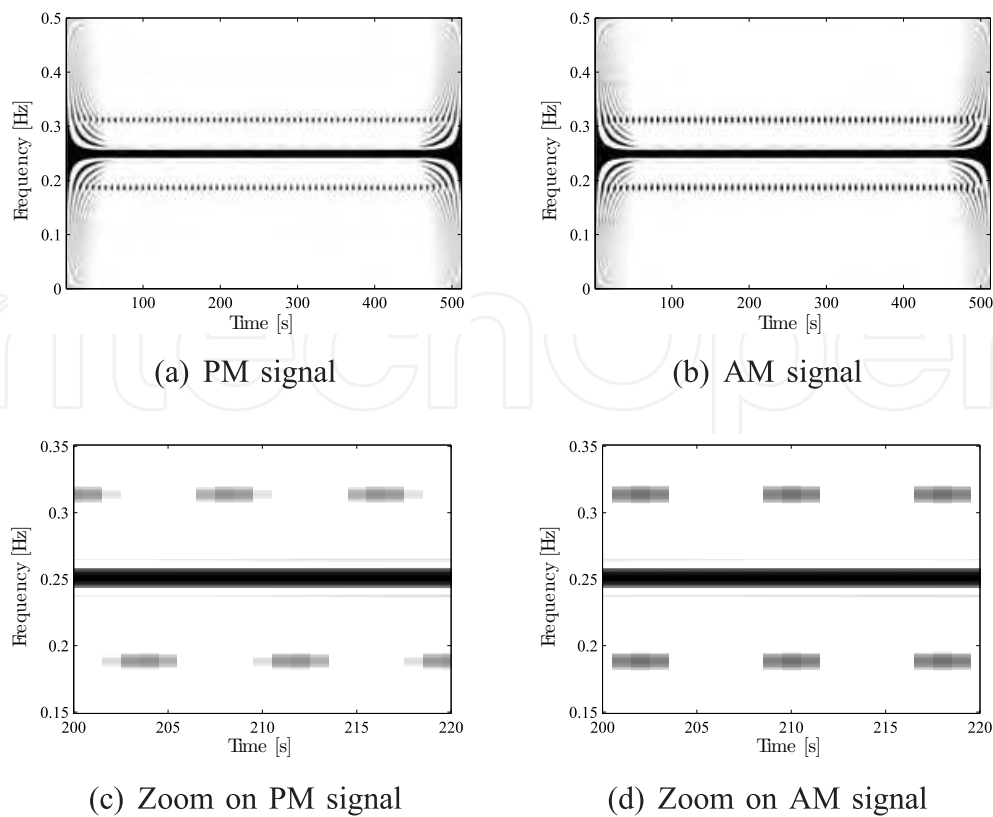
(d) Zoom on AM signal

Fig. 4. Pseudo Wigner Distribution of synthesized PM and AM signals with zoom on interference structure.

current signal is shown in Fig. 5. The linear evolution of the supply frequency is clearly visible apart from border effects. With the PM signal, oscillations at varying fault frequency $f_c(t)$ can be recognized. In case of the AM signal, no oscillations are present. Further IF and PWD analysis with automatic extraction of fault indicators is described in (Blödt, Bonacci, Regnier, Chabert & Faucher (2008)).

(a) PM signal
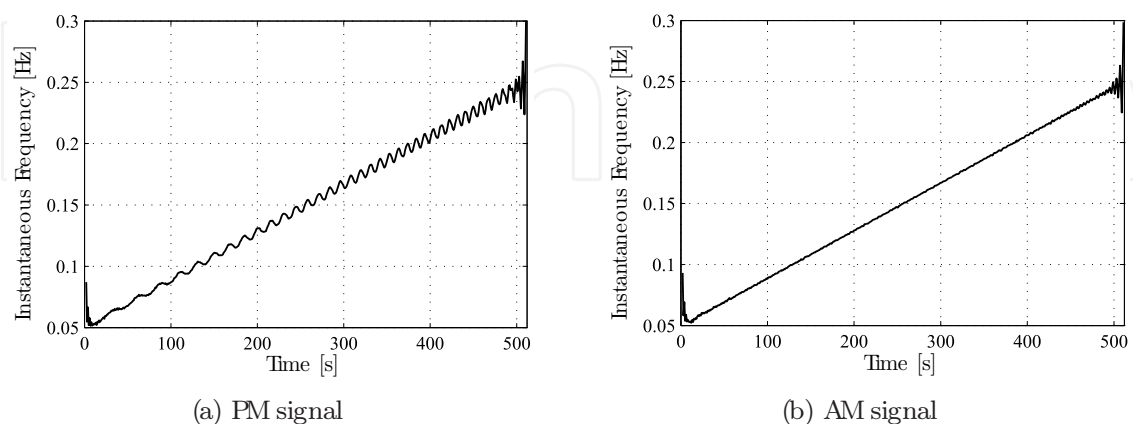
(b) AM signal

Fig. 5. Instantaneous frequency of simulated transient PM and AM signals.

3.5 Summary

Several signal processing methods suitable for the detection of mechanical faults by stator current analysis have been presented. Classical spectral analysis based on the PSD can give a first indication of a possible fault by an increase of sidebands at $f_s \pm f_r$. This method can only be applied in case of stationary signals without important variations of the supply frequency. The IF can be used to detect phase modulations since they lead to a time-varying IF. A global time-frequency signal analysis is possible using the WD or PWD where a characteristic interference structure appears in presence of the phase or amplitude modulations. The three methods have been illustrated with simulated signals.

4. Detection of dynamic airgap eccentricity and load torque oscillations under laboratory conditions

4.1 Experimental Setup

Laboratory tests have been performed on an experimental setup (see Fig.6) with a three phase, 400 V, 50 Hz, 5.5 kW Leroy Somer induction motor (motor A). The motor has $p = 2$ pole pairs and its nominal torque Γ_n is about 36 Nm. The machine is supplied by a standard industrial inverter operating in open-loop condition with a constant voltage to frequency ratio. The switching frequency is 3 kHz.

The load is a DC motor with separate, constant excitation connected to a resistor through a DC/DC buck converter. A standard PI controller regulates the DC motor armature current. Thus, using an appropriate current reference signal, a constant torque with a small additional oscillating component can be introduced. The sinusoidal oscillation is provided through a voltage controlled oscillator (VCO) linked to a speed sensor.

Since the produced load torque oscillations are not a realistic fault, load unbalance is also examined. Thereto, a mass is fixed on a disc mounted on the shaft. The torque oscillation produced by such a load unbalance is sinusoidal at shaft rotational frequency. With the chosen mass and distance, the torque oscillation amplitude is $\Gamma_c = 0.04$ Nm. If the motor bearings are healthy, the additional centrifugal forces created by the mass will not lead to airgap eccentricity.

A second induction motor with identical parameters has been modified to introduce dynamic airgap eccentricity (motor B). Therefore, the bearings have been replaced with bearings having a larger inner diameter. Then, eccentrical fitting sleeves have been inserted between the shaft and the inner race. The obtained degree of dynamic eccentricity is approximately 40%.

Measured quantities in the experimental setup include the stator voltages and currents, torque and shaft speed. The signals are simultaneously acquired through a 24 bit data acquisition board at 25 kHz sampling frequency. Further signal processing is done off-line with Matlab®.

4.2 Stator Current Spectrum Analysis

For illustration purposes, the stator current spectral signatures of a machine with dynamic eccentricity (motor B) are compared to an operation with load torque oscillations at frequency $f_c = f_r$ (motor A). In Fig. 7 the current spectrum of a motor with 40% dynamic eccentricity is compared to an operation with load torque oscillations of amplitude Γ_c=0.14 Nm. This corresponds to only 0.4% of the nominal torque. The healthy motor spectrum is also displayed and the average load is 10% of nominal load during this test. The stator current spectra show identical fault signatures around the fundamental frequency i.e. an increasing amplitude of the peaks at $f_s \pm f_r \approx 25$ Hz and 75 Hz. This behavior is identical under different load conditions.
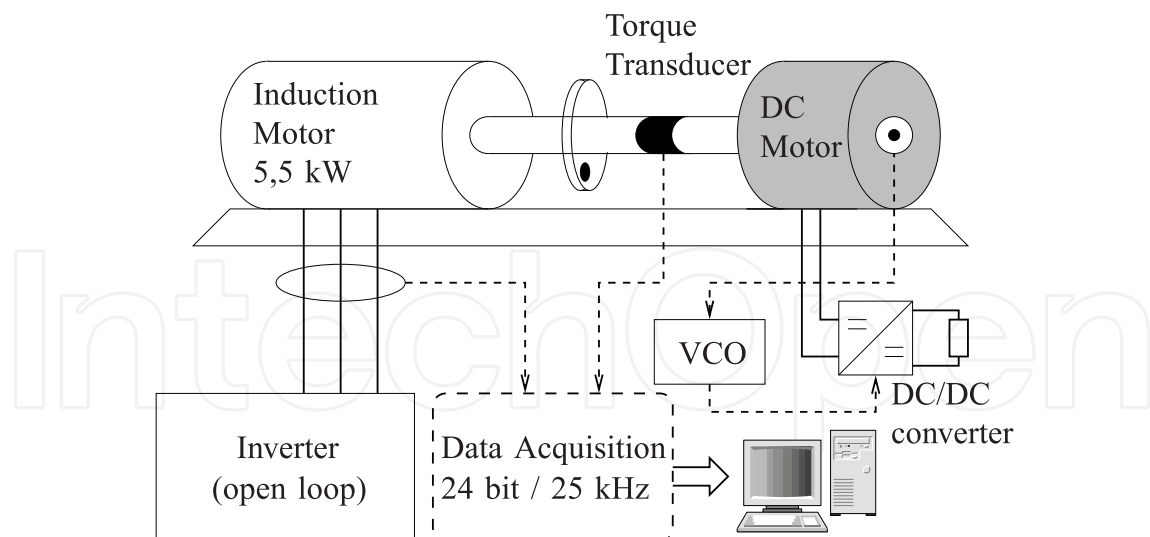
Fig. 6. Scheme of experimental setup

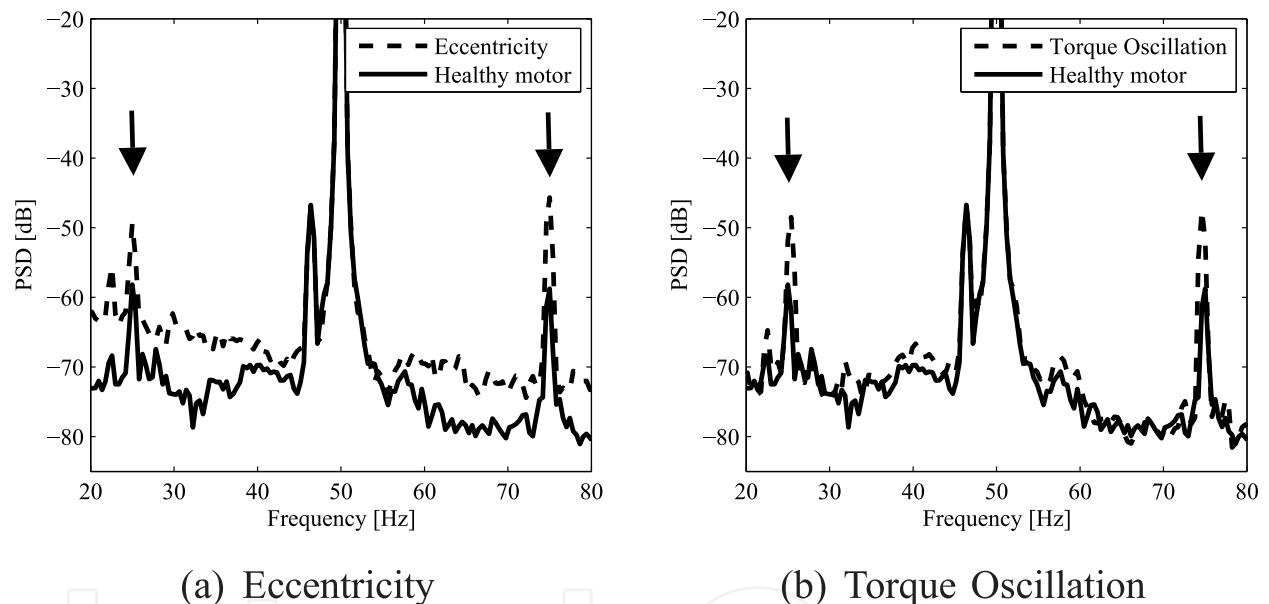(a) Eccentricity

(b) Torque Oscillation

Fig. 7. Comparison of experimental motor stator current spectra: 40 % eccentricity (B) vs. healthy machine (A) and 0.14 Nm load torque oscillation (A) vs. healthy machine (A) at 10% average load.

The stator current with load unbalance is analyzed in Fig. 8. A small weight has been fixed on the disc on the shaft and the amplitude of the introduced torque oscillation is $\Gamma_c = 0.04$ Nm. The load unbalance as a realistic fault also leads to a rise in sideband amplitudes at $f_s \pm f_r$.

These examples show that a monitoring strategy based on the spectral components $f_s \pm f_r$ can be used efficiently for detection purposes. In all three cases, these components show a considerable rise. However, this monitoring approach cannot distinguish between dynamic eccentricity and load torque oscillations.

In the following, transient stator current signals are also considered. They are obtained during motor startup between standstill and nominal supply frequency. The frequency sweep rate
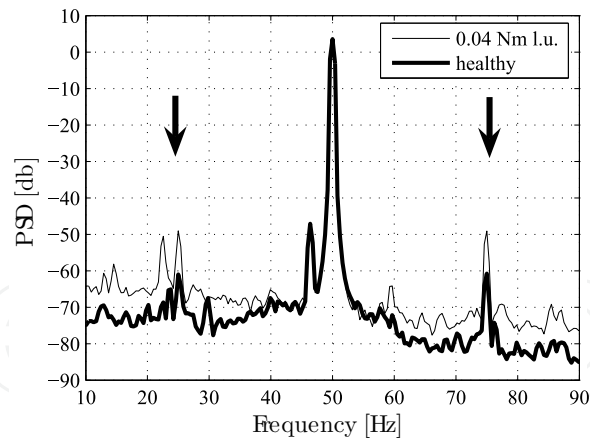
Fig. 8. PSD of stator current with load unbalance $\Gamma_c = 0.04$ Nm vs. healthy case

is 10 Hz per second i.e. the startup takes 5 seconds. For the following analysis, the transient between $f_s = 10$ Hz and 48 Hz is extracted. The PSD of a healthy and faulty transient signal are displayed in Fig. 9. This example illustrates that classic spectral estimation is not appropriate for transient signal analysis. The broad peak due to the time-varying supply frequency masks all other phenomena. The faulty and healthy case cannot be distinguished.
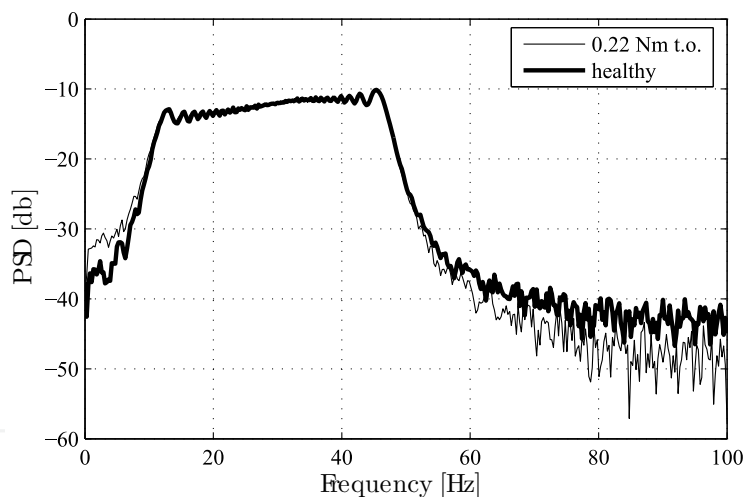
Fig. 9. PSD of stator current during speed transient with load torque oscillation $\Gamma_c = 0.22$ Nm vs. healthy case.

4.3 Stator Current Instantaneous Frequency Analysis
In this section, instantaneous frequency analysis will be applied to the stator current signals. The original signal has been lowpass filtered and downsampled to 200 Hz in order to remove high frequency content before time-frequency analysis. Only the information in a frequency range around the fundamental is conserved.

First, a transient stator current IF is shown in Fig. 10 for the healthy case and with a load torque oscillation $\Gamma_c = 0.5$ Nm. When load torque oscillations are present, the IF oscillations increase. The oscillation frequency is approximately half the supply frequency which corresponds to the shaft rotational frequency f_r.
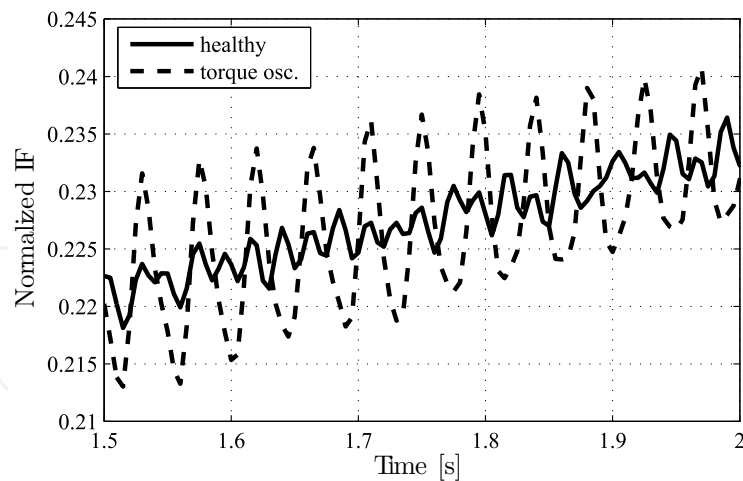
Fig. 10. Example of transient stator current IF with load torque oscillation ($\Gamma_c = 0.5$ Nm) vs. healthy case, 25% load.

For further analysis, the IF spectrogram can be employed. The spectrogram is a time-frequency signal analysis based on sliding short time Fourier transforms. More information can be found in (Boashash (2003)) (Flandrin (1999)). The two spectrograms depicted in Fig. 11 analyze the stator current IF during a motor startup with a small oscillation of $\Gamma_c = 0.22$ Nm and 10% average load. Besides the strong DC level at 0 Hz in the spectrogram, time varying components can already be noticed in the healthy case (a). They correspond to the supply frequency $f_s(t)$ and its second harmonic. Comparing the spectrogram of the healthy IF to the one with load torque oscillations (b), a fault-related component at $f_r(t)$ becomes clearly visible. More information about IF analysis can be found in (Blödt (2006)).

(a) healthy   (b) $\Gamma_c = 0.22$ Nm
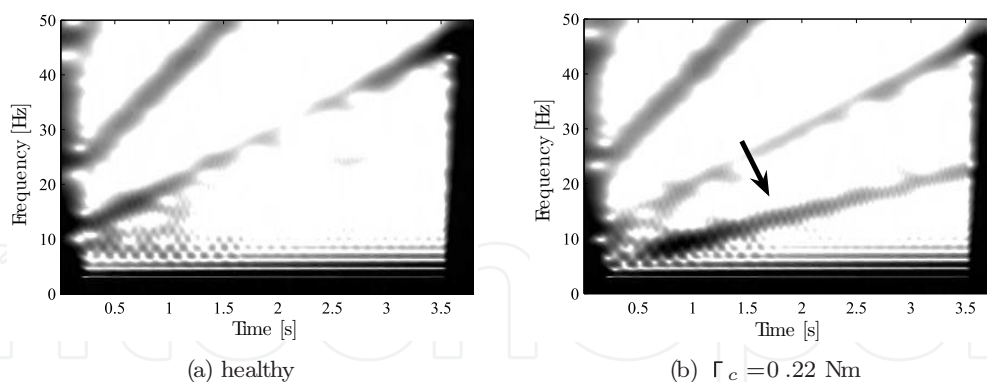
Fig. 11. Spectrogram of transient stator current IF with load torque oscillation $\Gamma_c = 0.22$ Nm vs. healthy case, 10% load.

4.4 Pseudo Wigner Distribution of Stator Current

The previously considered transient signals are also analyzed with the PWD. Figure 12 shows an example of the stator current PWD during a motor startup. Comparing the healthy case to 0.22 Nm load torque oscillations, the characteristic interference signature becomes visible around the time-varying fundamental frequency. Since the fault frequency is also time variable, the sideband location and their oscillation frequency depend on time (Blödt et al. (2005)).

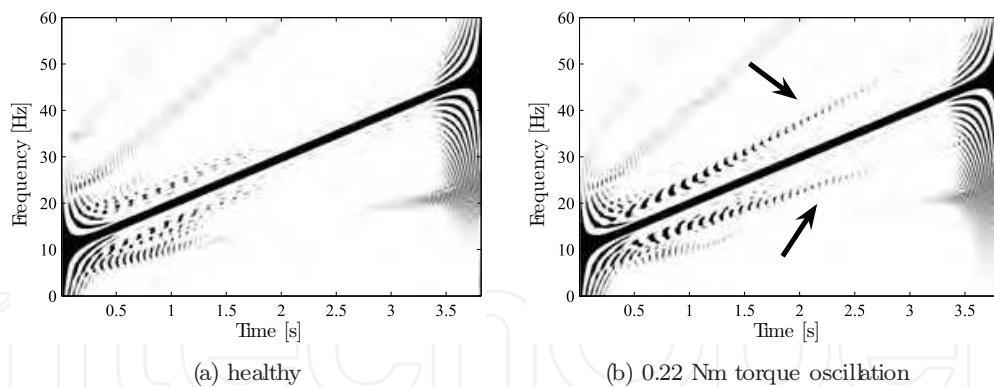(a) healthy   (b) 0.22 Nm torque oscillation

Fig. 12. PWD of transient stator current in healthy case and with load torque oscillation, 10% average load.

It is thereafter verified if dynamic eccentricity and load torque oscillations can be distinguished through the stator current PWD. The stator current PWDs with dynamic eccentricity and with 0.14 Nm load torque oscillation are shown in Fig. 13 for 10% average load. The characteristic fault signature is visible in both cases at $f_s \pm f_r/2 = 37.5$ Hz and 62.5 Hz. The phase shift between the upper and lower sideband seems closer to zero with eccentricity whereas with torque oscillations, it is closer to π. Nevertheless, it is difficult to determine the exact value from a visual analysis. However, the phase difference between the upper and lower sidebands can be automatically extracted from the PWD (see (Blödt, Regnier & Faucher (2006)). The result is about 125° with load torque oscillations and around 90° with dynamic eccentricity. These values differ from the theoretical ones (180° and 0° respectively) but this can be explained with load torque oscillations occurring as a consequence of dynamic eccentricity. A detailed discussion can be found in (Blödt, Regnier & Faucher (2006)). However, the phase shifts are sufficient to distinguish the two faults.
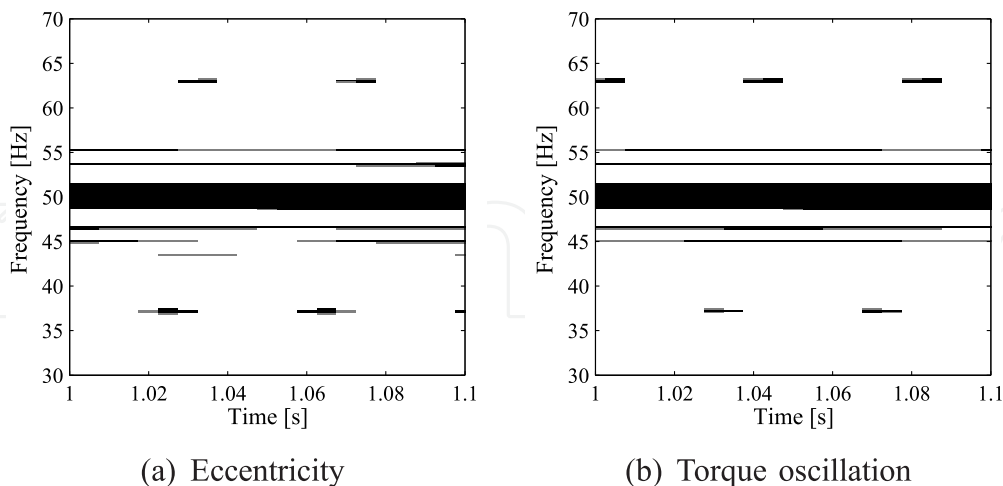

(a) Eccentricity   (b) Torque oscillation

Fig. 13. Detail of stator current PWD with 40% dynamic eccentricity (B) and 0.14 Nm load torque oscillation (A) at small average load

5. Detection of shaft misalignment in electric winches

5.1 Problem statement

Electric winches are widely used in industrial handling systems such has cranes, overhead cranes or hoisting gears. As illustrated in Fig. 14, they are usually composed of an induction machine driving a drum through gears. Different faults can occur on such systems, leading
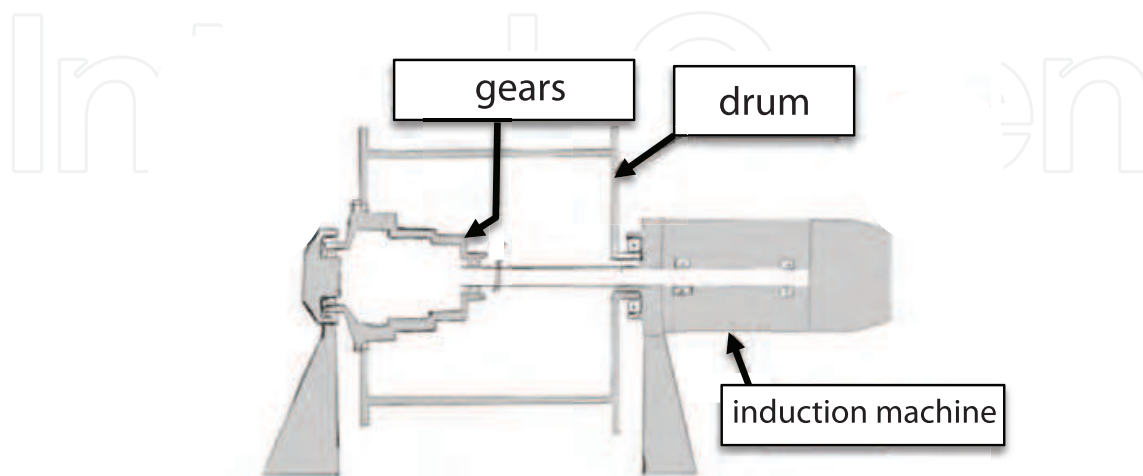
Fig. 14. Schematic representation of an electric winch.

to performance, reliability, and safety deterioration. A usual fault is the misalignment between the induction machine and the drum, generally due to strong radial forces applied to the drum by the handled load. Theoretical and experimental studies (see for example Xu & Marangoni (1994a;b)) show that such misalignments produce mechanical phenomena, which lead to torque oscillations and dynamic airgap eccentricity in the induction machine. It has been shown in section 2 that such phenomena generate amplitude and phase modulations in the supply currents of the machine. The goal of this part is to apply to these currents some of the signal processing tools presented in section 3 in order to detect a mechanical misalignment in the system. Therefore, this part is organized as follows : section 5.2 describes more precisely the fault and the necessary signal processing tools, and experimental results are finally presented in section 5.3.

5.2 Misalignment detection by stator current analysis

5.2.1 Shaft misalignment

Shaft misalignment is a frequent fault in rotating machinery, for which the shafts of the driving and the driven parts are not in the same centerline. The most general misalignment is a combination of angular misalignement (shaft centerlines do meet, but are not parallel) and offset misalignement (shaft centerlines are parallel, but do not meet). This type of fault generates reaction forces and torques in the coupling, and finally torque oscillations and dynamic airgap eccentricity in the driving machine. Moreover, these mechanical phenomena appear at even harmonics of the rotational frequencies of the driven parts (Xu & Marangoni (1994a)) (Xu & Marangoni (1994b)) (Sekhar & Prabhu (1995)) (Goodwin (1989)). For example, in the case of a misalignment of the winch shafts described in Fig. 14, torque oscillations and dynamic eccentricity are generated at even harmonics of the rotational frequencies of the induction machine, the gearbox and also the drum.

Mechanical fault detection in induction motor drives through stator
current monitoring - Theory and application examples
469

The theoretical model developed in sections 2.1 and 2.2 describes how mechanical phenomena are "seen" by an induction machine in its supply currents. More precisely, it has been shown that torque oscillations cause phase modulation of the stator current components (see Eq. (13)), while airgap eccentricity causes amplitude modulation (see Eq. (21)).

Therefore, in the case of a shaft misalignment in a system similar to Fig. 14, amplitude and phase modulations appear in the supply currents of the induction machine, and these modulations have frequencies equal to even harmonics of the rotational frequencies of the driving machine, the gearbox and the drum. Finally, the modulations generated by the drum are much more easy to detect since its rotational frequency is generally much lower than the supply and rotational frequencies of the machine f_s and f_r. In the following, only such low frequency modulations will be examined.

5.2.2 Shaft misalignment detection

The previous section has described that it should be possible to detect a shaft misalignment in an electric winch by analyzing its supply currents. Indeed, one only has to detect a significant increase in the amplitude and phase modulations of their fundamental component. A simple possibility is to analyze the variations of its instantaneous amplitude and instantaneous frequency, defined in section 3. These quantities can be easily real-time estimated as shown in (A. Reilly & Boashash (1994)), and Fig. 15 briefly describes the principle of this approach.
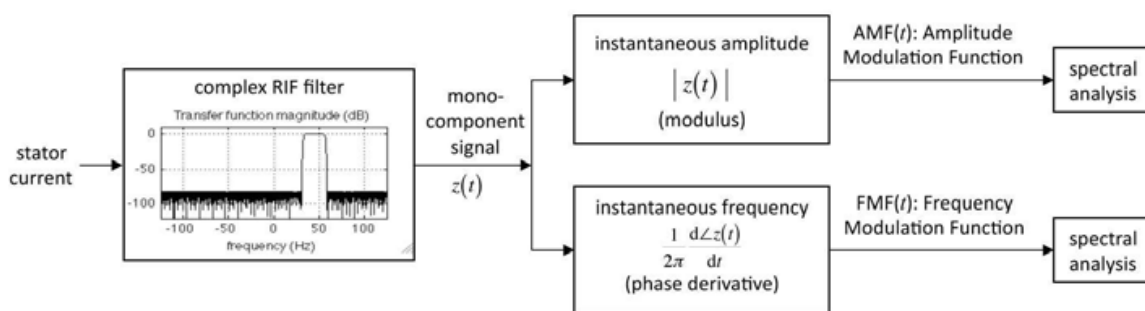

Fig. 15. Stator current analysis method for shaft misalignment detection.

First of all, one of the stator currents is filtered by a bandpass filter in order to obtain the fundamental component only, without any other component. The filter used in this application has a passband only situated in the positive frequency domain around $+f_s$ with $f_s = 45.05$ Hz (see the transfer function in Fig. 15) in order to directly obtain the analytical part of the analyzed signal, as explained in (A. Reilly & Boashash (1994)). The transfer function $H(f)$ of this filter is therefore not hermitian ($H(f) \neq H^*(-f)$), and its impulse response is complex-valued. This particularity is not problematic concerning the real-time implementation of this filter, since its finite impulse response only needs twice as many coefficients as a classical real-valued finite impulse response filter. Finally, the output of this filter is a complex-valued monocomponent signal $z(t)$ which represents the analytical part of the supply current fundamental component. In a second step, the modulus and the phase derivative of this complex signal lead to the instantaneous amplitude and frequency to estimate. Once their mean value substracted, these quantities are called amplitude modulation function (AMF) and frequency modulation function (FMF). They correspond to instantaneous amplitude and frequency variations of the current fundamental component and contain the researched modulations. Finally, power spectral densities of the AMF and FMF are estimated in order to detect and identify such modulations.

5.3 Experimental results

5.3.1 Test bench and operating conditions

A test bench has been designed by the CETIM (French CEntre Technique des Industries Mécaniques) in order to simulate different types of faults occuring in industrial handling systems (Sieg-Zieba & Tructin (2008)). It is composed of two 22 kW Potain electric winches, and one cable winding up from one winch to the other through a pulley as shown in Fig. 16.
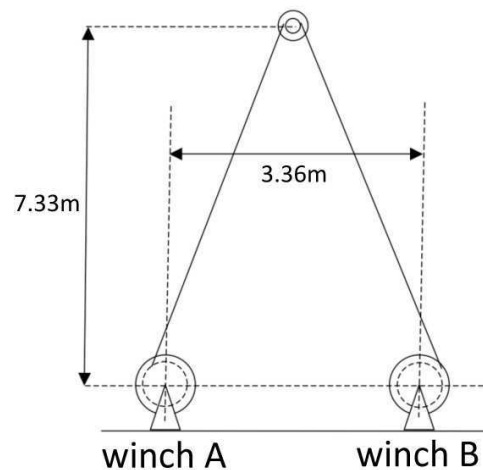

Fig. 16. Schematic description of the test bench.

The two winches are constituted as shown in Fig. 14, and the winch A is controlled through an inverter as a driving winch, while the winch B is only used to apply a predetermined mechanical load. The winch A is equipped with current probes in order to measure the stator currents of its induction machine. Moreover, an angular misalignment can be obtained on the same winch by inserting a shim with a slope between the motor flange and the drum bearing housing, thus creating an angle of $0.75°$ while the tolerance of the coupling is $0.5°$.

During the experiments, the signals were recorded during 80 s at a sampling frequency of 25 kHz under stationary working conditions with and without misalignment. The constant mechanical load applied by the winch B was 2000 daN, and the rotational frequency reference value of the induction machine of the winch A was $f_r = 23$ Hz. These conditions resulted in a fundamental supply frequency of $f_s = 45.05$ Hz, and a drum rotational frequency of $f_{r_d} = 0.29$ Hz.

5.3.2 Results

Experimental results presented in this section have been obtained by applying the method developed in section 5.2 to a supply current measured under the operating conditions described in the previous section. The proposed method leads to the estimation of the AMF and FMF of the stator current fundamental component, and the performance of this method is illustrated by the power spectral densities of these two functions. Low-frequency spectral contents of the AMF and FMF are respectively represented in Fig. 17 and 18. The power spectral densities obtained without any misalignment are in dashed line, while they are in solid line in case of misalignment.

As expected, amplitude and frequency modulations strongly increase in the low-frequency range when a shaft misalignment occurs, and more precisely at even harmonics of the drum rotational frequency (see arrows in Fig. 17 and 18 around $2 \times f_{r_d} = 0.58$ Hz and $4 \times f_{r_d} =$
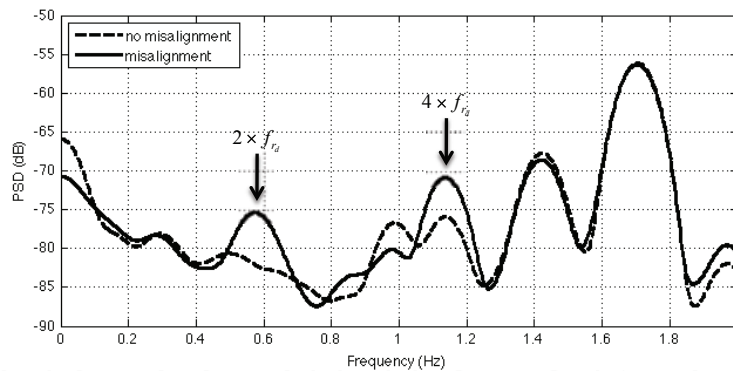
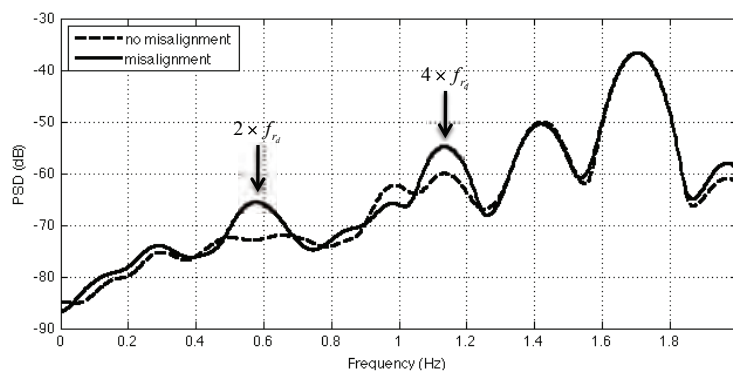Fig. 17. Power spectral density of the AMF with (-) and without (- -) misalignment.

Fig. 18. Power spectral density of the FMF with (-) and without (- -) misalignment.

1.16 Hz). These results clearly show that a potential misalignment in an electric winch can be detected by analyzing its supply currents.

Furthermore, a simple and efficient misalignment detector can be derived from AMF and FMF power spectral densities. For example, the power increase of AMF and FMF in a frequency band corresponding to the expected fault can easily be estimated from these quantities by integration. In the present case, the power of these two modulation functions between 0.25 Hz and 1.25 Hz (a frequency band containing $2 \times f_{r_d}$ and $4 \times f_{r_d}$) increases of about 80% (for AMF) and 120% (for FMF) when a misalignment occurs. Finally, it can be noted that such a detector can be easily real-time implemented since it is based on real-time operations only (see Fig. 15).

5.4 Conclusion
This section has shown that a shaft misalignment in an electric winch can be detected by analyzing its supply currents. Experimental results confirm that a misalignment generates additional amplitude and frequency modulations in stator currents. These phenomena can be easily detected and characterized by analyzing the spectral content of amplitude and frequency modulation functions of the stator current fundamental component. For example, Fig. 17 and 18 show that these additional modulations occur at even harmonics of the drum rotational frequency, *i.e.* in a very low-frequency range. Finally, a simple and efficient real-time detector has been proposed, based on the integration of the power spectral densities of the AMF and FMF.

6. Detection of single point bearing defects

The following section considers the detection of single point bearing defects in induction motors. Bearing faults are the most frequent faults in electric motors (41%) according to an IEEE motor reliability study for large motors above 200 HP (IEEE Motor reliability working group (1985b)), followed by stator (37%) and rotor faults (10%). Therefore, their detection is of great concern. First, some general information about bearing geometry and characteristic frequencies will be given. Then, a theoretical study of bearing fault effects on the stator current is presented (see Blödt, Granjon, Raison & Rostaing (2008)). Finally, experimental results illustrate and validate the theoretical approach.

6.1 Bearing Fault Types

This paper considers rolling-element bearings with a geometry shown in Fig. 19. The bearing consists mainly of the outer and inner raceway, the balls and the cage which assures equidistance between the balls. The number of balls is denoted N_b, their diameter is D_b and the pitch or cage diameter is D_c. The point of contact between a ball and the raceway is characterized by the contact angle β.

Bearing faults can be categorized into distributed and localized defects (Tandon & Choudhury (1997)) (Stack et al. (2004b)). Distributed defects affect a whole region and are difficult to characterize by distinct frequencies. In contrast, single-point defects are localized and can be classified according to the affected element:

- outer raceway defect

- inner raceway defect

- ball defect

A single point defect could be imagined as a small hole, a pit or a missing piece of material on the corresponding element. Only these are considered in the following.

6.2 Characteristic Fault Frequencies

With each type of bearing fault, a characteristic fault frequency f_c can be associated. This frequency is equivalent to the periodicity by which an anomaly appears due to the existence of the fault. Imagining for example a hole on the outer raceway: as the rolling elements move over the defect, they are regularly in contact with the hole which produces an effect on the machine at a given frequency.

The characteristic frequencies are functions of the bearing geometry and the mechanical rotor frequency f_r. A detailed calculation of these frequencies can be found in (Li et al. (2000)). For the three considered fault types, f_c takes the following expressions:

$$\text{Outer raceway:} \qquad f_o = \frac{N_b}{2} f_r \left(1 - \frac{D_b}{D_c} \cos \beta \right) \qquad (35)$$

$$\text{Inner raceway:} \qquad f_i = \frac{N_b}{2} f_r \left(1 + \frac{D_b}{D_c} \cos \beta \right) \qquad (36)$$

$$\text{Ball:} \qquad f_b = \frac{D_c}{D_b} f_r \left(1 - \frac{D_b^2}{D_c^2} \cos^2 \beta \right) \qquad (37)$$

It has been statistically shown in (Schiltz (1990)) that the vibration frequencies can be approximated for most bearings with between six and twelve balls by :

$$f_o = 0.4\, N_b f_r \tag{38}$$
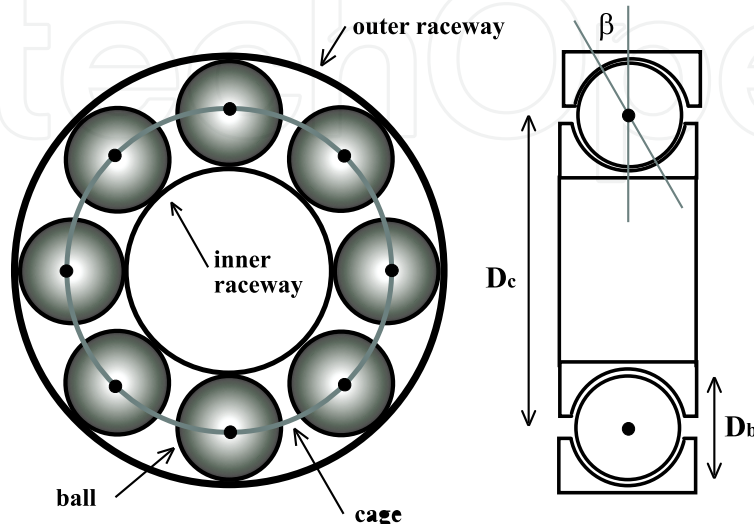$$f_i = 0.6\, N_b f_r \tag{39}$$

Fig. 19. Geometry of a rolling-element bearing.

6.3 Short Literature Survey on Bearing Fault Detection by Stator Current Analysis

Vibration measurement is traditionally used to detect bearing defects. Analytical models describing the vibration response of a bearing with single point defects can be found in (Tandon & Choudhury (1997)) (MacFadden & Smith (1984)) (Wang & Kootsookos (1998)). The most often quoted model studying the influence of bearing damage on the induction machine's stator current was proposed by R. R. Schoen et al. in (Schoen et al. (1995)). The authors consider the generation of rotating eccentricities at bearing fault characteristic frequencies f_c which leads to periodical changes in the machine inductances. This should produce additional frequencies f_{bf} in the stator current given by:

$$f_{bf} = |f_s \pm k f_c| \tag{40}$$

where f_s is the electrical stator supply frequency and $k = 1, 2, 3, \ldots$.
A general review about bearing fault detection by stator current monitoring can be found in (Zhou et al. (2007)). Stack examines in (Stack et al. (2004b)) single point defects and generalized roughness. In (Stack et al. (2004a)), the stator current is analyzed using parametric spectrum analysis such as autoregressive modelling. Neural network techniques and the wavelet transform are used in (Eren et al. (2004)) for bearing fault detection and wavelet decomposition is applied in the case of variable speed drives in (Teotrakool et al. (2006)). In (Zhou et al. (2008)) stator current noise cancellation techniques are described for bearing fault detection.
In the following, a detailed theoretical study will be conducted to analyze the physical effects of bearing faults on the induction machine and the stator current. This will yield additional stator current frequencies with respect to the existing model and will give insight on the modulation type.

6.4 Theoretical Study of Single Point Bearing Defects

Two physical effects are considered in the theoretical study when the single point defect comes into contact with another bearing element:

1. the introduction of a radial movement of the rotor center,

2. the apparition of load torque variations.

The method used to study the influence of the rotor displacement on the stator current is again based on the MMF (magnetomotive force) and permeance wave approach (see section 2). The following model relies on several simplifying assumptions. First, load zone effects in the bearing are not considered. The fault impact on the airgap length is considered by a series of Dirac generalized functions. In reality, the fault generates other pulse shapes, but this alters only the harmonic amplitudes. Since this modeling approach focusses on the frequency combinations and modulation types and not on exact amplitudes, this assumption is reasonable. The calculation of the airgap magnetic field does not take into account higher order space and time harmonics for the sake of simplicity. However, the calculated modulation effects affect higher harmonics in the same way as the fundamental. As before, higher order armature reactions are also neglected.

6.4.1 Airgap Length Variations

The first step in the theoretical analysis is the determination of the airgap length g as a function of time t and angular position θ in the stator reference frame. The radial rotor movement causes the airgap length to vary as a function of the defect, which is always considered as a hole or a point of missing material in the corresponding bearing element.

6.4.1.1 Outer Race Defect

Without loss of generality, the outer race defect can be assumed to be located at the angular position $\theta = 0$. When there is no contact between a ball and the defect, the rotor is perfectly centered. In this case, the airgap length g is supposed to take the constant value g_0, neglecting rotor and stator slotting effects. On the contrary, every $t = k/f_o$ (with k integer), the contact between a ball and the defect leads to a small movement of the rotor center in the stator reference frame (see Fig. 20). In this case, the airgap length can be approximated by $g_0(1 - e_o \cos\theta)$, where e_o is the relative degree of eccentricity. In order to model the fault impact on the airgap length as a function of time, a series of Dirac generalized functions can then be used as it is common in models for vibration analysis (MacFadden & Smith (1984)).

These considerations lead to the following expression for the airgap length:

$$g_o(\theta, t) = g_0 \left[1 - e_o \cos(\theta) \sum_{k=-\infty}^{+\infty} \delta\left(t - \frac{k}{f_o} \right) \right] \tag{41}$$

where e_o is the relative degree of eccentricity introduced by the outer race defect. This equation can be interpreted as a temporary static eccentricity of the rotor, appearing only at $t = k/f_o$. The function $g_o(\theta, t)$ is represented in Fig. 21 for $\theta = 0$ as an example.

6.4.1.2 Inner Race Defect

In this case, the situation is slightly different from the outer race defect. The fault occurs at the instants $t = k/f_i$. As the defect is located on the inner race, the angular position of the minimal airgap length moves with respect to the stator reference frame as the rotor turns at
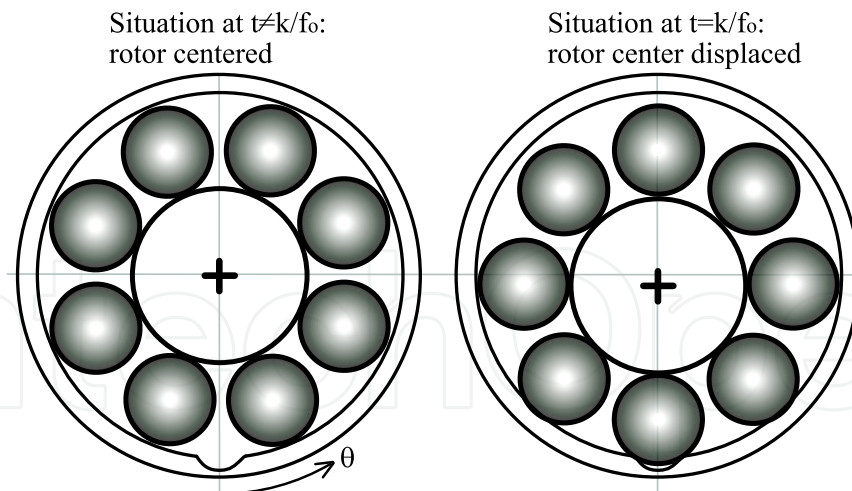
Situation at $t \neq k/f_o$:
rotor centered

Situation at $t = k/f_o$:
rotor center displaced

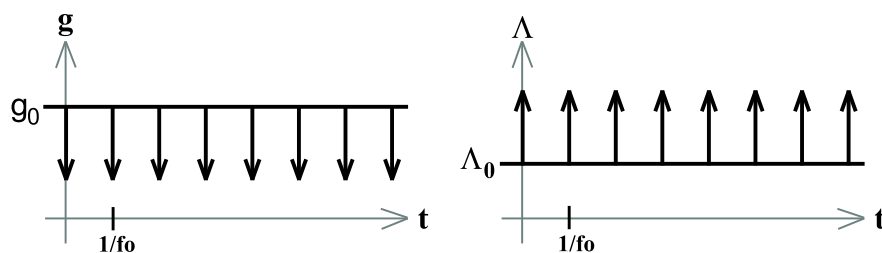Fig. 20. Radial rotor movement due to an outer bearing raceway defect.

Fig. 21. Airgap length g and permeance Λ in the presence of an outer bearing raceway defect for $\theta = 0$.

the angular frequency ω_r (see Fig. 22). Between two contacts with the defect, the defect itself has moved by an angle described by:

$$\Delta \theta_i = \omega_r \Delta t = \frac{\omega_r}{f_i} \tag{42}$$

Hence, equation (41) becomes:

$$g_i(\theta, t) = g_0 \left[1 - e_i \sum_{k=-\infty}^{+\infty} \cos(\theta + k\Delta\theta_i) \delta \left(t - \frac{k}{f_i} \right) \right] \tag{43}$$

where e_i is the relative degree of eccentricity introduced by the inner race defect.

This equation can be simplified for further calculations by extracting the cosine-term of the sum so that the series of Dirac generalized functions may be later developed into a Fourier series. One fundamental property of the Dirac generalized function is given by the following equation (Max & Lacoume (2000)):

$$h(k) \cdot \delta \left(t - \frac{k}{f_i} \right) = h(tf_i) \cdot \delta \left(t - \frac{k}{f_i} \right) \tag{44}$$

This formula becomes obvious when one considers that $\delta(t - k/f_i)$ always equals 0, except for $t = k/f_i$. After combining (44), (43) and (42), the airgap length becomes:

$$g_i(\theta, t) = g_0 \left[1 - e_i \cos(\theta + \omega_r t) \sum_{k=-\infty}^{+\infty} \delta \left(t - \frac{k}{f_i} \right) \right] \tag{45}$$
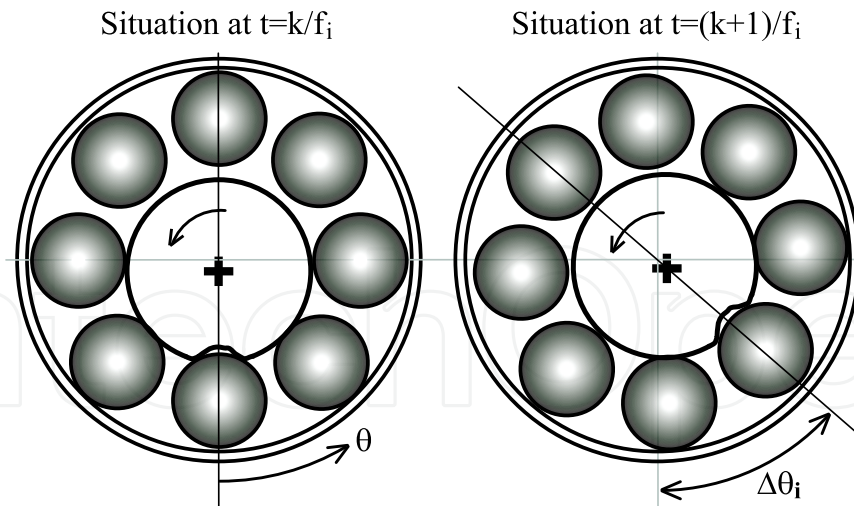
Fig. 22. Radial rotor movement due to an inner bearing raceway defect.

6.4.1.3 Ball Defect

In presence of ball defect, the defect location moves in a similar way as the inner raceway fault. The fault causes an anomaly on the airgap length at the instants $t = k/f_b$. The angular position of minimal airgap length changes in function of the cage rotational frequency. Actually, the balls are all fixed in the cage which rotates at the fundamental cage frequency ω_{cage}, given by (Li et al. (2000)):

$$\omega_{cage} = \frac{1}{2}\omega_r \left(1 - \frac{D_b}{D_c}\cos\beta \right) \tag{46}$$

The angle $\Delta\theta_b$ by which the fault location has moved between two fault impacts becomes:

$$\Delta\theta_b = \omega_{cage}\Delta t = \frac{\omega_{cage}}{f_b} \tag{47}$$

By analogy with (45), the expression of airgap length in presence of a ball defect becomes:

$$g_b(\theta, t) = g_0 \left[1 - e_b\cos\left(\theta + \omega_{cage}t\right) \sum_{k=-\infty}^{+\infty} \delta\left(t - \frac{k}{f_b}\right) \right] \tag{48}$$

where e_b is the relative degree of eccentricity introduced by the ball defect.

6.4.1.4 Generalization

In order to simplify the following considerations, equations (41), (45) and (48) can be combined in a generalized expression for the airgap length g in presence of a bearing fault:

$$g(\theta, t) = g_0 \left[1 - e\cos\left(\theta + \psi(t)\right) \sum_{k=-\infty}^{+\infty} \delta\left(t - \frac{k}{f_c}\right) \right] \tag{49}$$

where f_c is the characteristic bearing fault frequency given by (35), (36) or (37), and $\psi(t)$ is defined as follows:

$$\psi(t) = \begin{cases} 0 & \text{for an outer race defect} \\ \omega_r t & \text{for an inner race defect} \\ \omega_{cage}t & \text{for a ball defect} \end{cases} \tag{50}$$

6.4.2 Airgap Permeance

The airgap permeance Λ is proportional to the inverse of the airgap length g and is defined as follows:

$$\Lambda = \frac{\mu}{g} \tag{51}$$

where $\mu = \mu_r \mu_0$ is the magnetic permeability of the airgap. In the case of a bearing fault, the permeance becomes with (49):

$$\Lambda(\theta, t) = \Lambda_0 \frac{1}{\left[1 - e\cos\left(\theta + \psi(t)\right) \sum\limits_{k=-\infty}^{+\infty} \delta\left(t - \frac{k}{f_c}\right)\right]} \tag{52}$$

where $\Lambda_0 = \mu/g_0$. The relationship between airgap length $g(\theta, t)$ and airgap permeance $\Lambda(\theta, t)$ is illustrated on Fig. 21 at the position $\theta = 0$ for an outer raceway defect.

Firstly, in order to simplify this expression, the fraction $1/(1-x)$ is approximated for small airgap variations by the first order term of its series development:

$$\frac{1}{1-x} = 1 + x + x^2 + x^3 + \dots \qquad \text{for } |x| < 1$$
$$\approx 1 + x \tag{53}$$

The condition $|x| < 1$ is always satisfied because the degree of eccentricity verifies $|e| < 1$ in order to avoid contact between rotor and stator.

Secondly, the series of Dirac generalized functions is expressed as a complex Fourier series development (Max & Lacoume (2000)):

$$\sum_{k=-\infty}^{+\infty} \delta\left(t - \frac{k}{f_c}\right) = \sum_{k=-\infty}^{+\infty} c_k e^{-j2\pi k f_c t}$$
$$= c_0 + 2 \sum_{k=1}^{+\infty} c_k \cos\left(2\pi k f_c t\right) \tag{54}$$

with the Fourier series coefficients $c_k = f_c \; \forall k$.

Equations (52), (53) and (54) can be combined into a simplified expression for the airgap permeance wave:

$$\Lambda(\theta, t) \approx \Lambda_0 \Big\{ 1 + ec_0 \cos\left(\theta + \psi(t)\right)$$
$$+ e \sum_{k=1}^{+\infty} c_k \cos\left(\theta + \psi(t) + k\omega_c t\right)$$
$$+ e \sum_{k=1}^{+\infty} c_k \cos\left(\theta + \psi(t) - k\omega_c t\right) \Big\} \tag{55}$$

6.4.3 Airgap Flux Density

The total fundamental MMF wave F_{tot} is assumed:

$$F_{tot}(\theta,t) = F\cos(p\theta - \omega_s t + \varphi) \tag{56}$$

Multiplication of (55) and (56) leads to the expression of the flux density distribution $B_{tot}(\theta,t)$:

$$\begin{aligned}
B_{tot}(\theta,t) &= F_{tot}(\theta,t) \cdot \Lambda(\theta,t) \\
&= F\Lambda_0 \cos(p\theta - \omega_s t + \varphi) \\
&+ \sum_{k=0}^{\infty} B_k \Big[\cos\big((p\pm 1)\theta \pm \psi(t) \pm k\omega_c t - \omega_s t + \varphi\big)\Big]
\end{aligned} \tag{57}$$

where B_k are the amplitudes of the fault-related flux density waves. The notation $\pm$ is used to write all possible frequency combinations in a compact form.

Equation (57) clearly shows the influence of the rotor displacement caused by the bearing fault on the flux density. In addition to the fundamental sine wave (term B_0), a multitude of fault-related sine waves appear in the airgap. These supplementary waves have $p \pm 1$ pole pairs and a frequency content f_{ecc} given by:

$$f_{ecc} = \frac{1}{2\pi}\left(\pm\frac{d\psi(t)}{dt} \pm k\omega_c - \omega_s\right) \tag{58}$$

6.4.4 Stator Current

The additional flux density components according to (57) are equivalent to an additional magnetic flux $\Phi(\theta,t)$. By considering the realization of the winding and the geometry of the machine, the additional flux $\Phi(t)$ in each stator phase can be obtained. If the stator voltages are imposed, the time varying flux causes additional components in the motor stator current according to the stator voltage equation for the phase m:

$$V_m(t) = R_s I_m(t) + \frac{d\Phi_m(t)}{dt} \tag{59}$$

The frequency content of the flux in each phase is supposed to be equal to the frequency content of the airgap field according to (58). Under the hypothesis of imposed stator voltages, the stator current in each phase is given by the derivative of the corresponding flux. This leads to the following expression for the stator current $I_m(t)$ with ω_r supposed constant:

$$I_m(t) = \sum_{k=0}^{\infty} I_k \cos\big[\pm\psi(t) \pm k\omega_c t - \omega_s t + \varphi_m\big] \tag{60}$$

It becomes thus obvious, that the radial rotor movement due to the bearing fault results in additional frequencies in the stator current. With the three fault types, these frequencies are obtained from (50) and (60):

Outer race defect: $\qquad\qquad f_{ecc\ or} = f_s \pm k f_o \tag{61}$

Inner race defect: $\qquad\qquad f_{ecc\ ir} = f_s \pm f_r \pm k f_i \tag{62}$

Ball defect: $\qquad\qquad f_{ecc\ ball} = f_s \pm f_{cage} \pm k f_b \tag{63}$

where $k = 1,2,3,\ldots$. In terms of signal processing, it can be noticed that the effect of the fault related rotor movement on the stator current is an amplitude modulation of the fundamental sine wave, due to the effect of the modified permeance on the fundamental MMF wave.

Mechanical fault detection in induction motor drives through stator
current monitoring - Theory and application examples
479

	Eccentricity	Torque oscillations
Outer raceway	$f_s \pm k f_o$	$f_s \pm k f_o$
Inner raceway	$f_s \pm f_r \pm k f_i$	$f_s \pm k f_i$
Ball defect	$f_s \pm f_{cage} \pm k f_b$	$f_s \pm k f_b$

Table 1. Summary of bearing fault related frequencies in the stator current spectrum

6.4.5 Load torque oscillations

In this section, the second considered effect of a bearing fault on the machine is studied. Imagining for example a hole in the outer race: each time a ball passes in a hole, a mechanical resistance will appear when the ball tries to leave the hole. The consequence is a small increase of the load torque at each contact between the defect and another bearing element. The bearing fault related torque variations appear at the previously mentioned characteristic vibration frequencies f_c (see section 6.2) as they are both of same origin: a contact between the defect and another element.

The effect of load torque oscillations on the stator current has already been studied in section 2.1. The torque oscillations resulting from single point bearing defects will result in the same stator current phase modulations as described in equation (13). Note that the fault characteristic frequency f_c will be take values depending on the fault type defined in section 6.2.

6.5 Summary

The results from the preceding theoretical study enlarge the existing model of the effects of bearing faults on stator current. The frequencies that can be found when the stator current PSD is analyzed, are resumed in Table 1.

6.6 Experimental Results

6.6.1 Description of Experimental Setup

The experimental tests were carried out on a test rig with a standard 1.1 kW, 2-pole pair, Y-coupled induction motor. A DC-machine was used to simulate different load levels. In order to reduce harmonic content in the supply voltage, the induction motor is directly fed by a synchronous generator (100 kVA) working as a generator. Measured quantities are the three line currents, the stator voltages, motor speed, torque and two vibration signals issued from piezoelectric accelerometers mounted on the stator core. Data are sampled at 16 kHz and processed using Matlab$^{\circledR}$.

Two classes of faulty bearings (NSK 6205) are available. First, new bearings have been damaged artificially to produce defects on the outer and inner raceway. The defects consist of holes that have been drilled axially through the raceways (see Fig. 23). Secondly, bearings with realistic damage were tested, issued from industrial maintenance. The faulty bearings are mounted at the load-end of the induction machine.

The characteristic vibration frequencies take the following values at no-load operation: outer raceway frequency $f_o = 89.6$ Hz, inner raceway frequency $f_i = 135.4$ Hz, ball frequency $f_b = 58.8$ Hz. The contact angle has been assumed to be $\beta = 0$.

6.6.2 Outer Raceway Defect

The defect on the outer raceway has already been experimentally studied in (Schoen et al. (1995)), so that it will be discussed very shortly. During the tests, the characteristic vibration

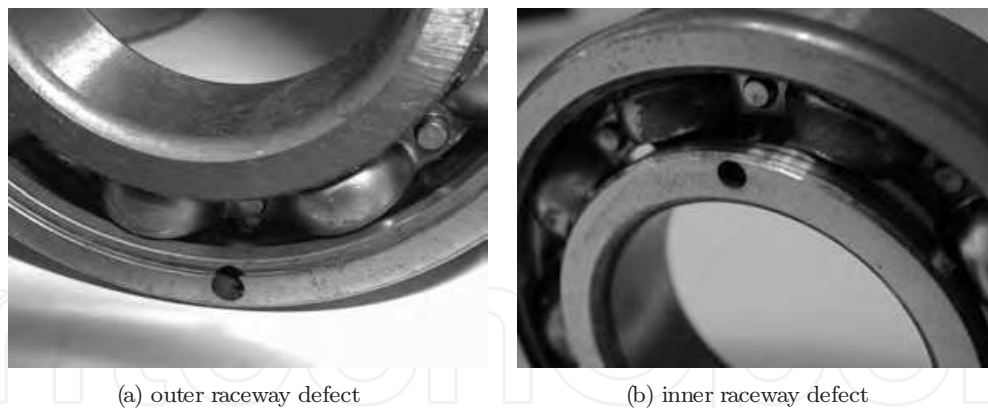(a) outer raceway defect   (b) inner raceway defect

Fig. 23. Photo of bearings with single point defects

frequency and its multiples were clearly visible on the vibration spectrum of the machine. There also appeared torque oscillations at the characteristic vibration frequencies.

The current spectrum shows a characteristic component at 125 Hz which corresponds to the frequency combination $|f_s - 2f_o|$ (see Fig. 24). It is interesting to note, that the same frequency combination appeared in (Bonaldi et al. (2002)) where a bearing with an outer race defect was tested experimentally.
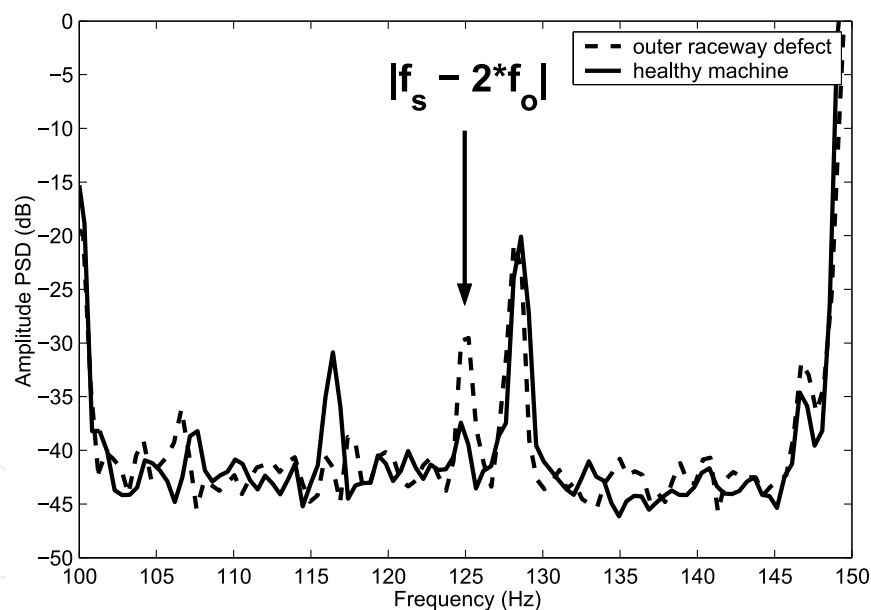
Fig. 24. Stator current spectrum of loaded machine with outer raceway defect.

6.6.3 Inner Raceway Defect

In a first step, the vibration signal is analyzed. A logarithmic plot of the vibration spectrum with a damaged bearing in comparison with the healthy machine condition is shown in Fig. 25. The characteristic frequency of the inner raceway defect f_i and its multiples (e.g. $2f_i$) are the components with the largest magnitude. Multiple tests with different load levels permitted to observe slight variations of the characteristic vibration frequency according to equation (36). Additional components due to other mechanical effects e.g. the cage rotational frequency

Mechanical fault detection in induction motor drives through stator
current monitoring - Theory and application examples
481

(≈ 10 Hz) and a general rise of the vibration level can also be noticed on the vibration spectrum.
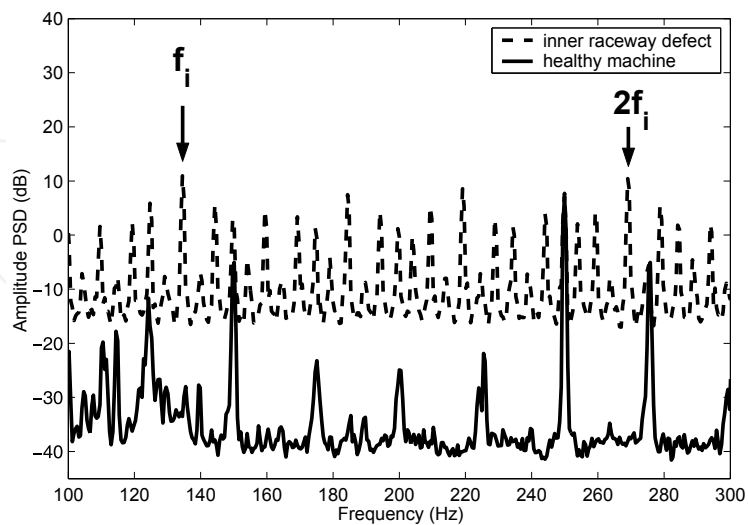

Fig. 25. Vibration spectrum of unloaded machine with inner raceway defect.

A spectral analysis of the measured load torque is shown in Fig. 26. The characteristic fault frequency f_i clearly appears on the torque spectrum with an amplitude of +15 dB in comparison to the healthy case. This validates the proposed theoretical approach which assumes torque variations at the characteristic frequency as a consequence of the bearing fault. Higher harmonics of f_i can also be observed. In addition to the mentioned components, other frequencies appear in the torque spectrum at e.g. 110 and 115 Hz, but they have no direct link to a predicted characteristic frequency.
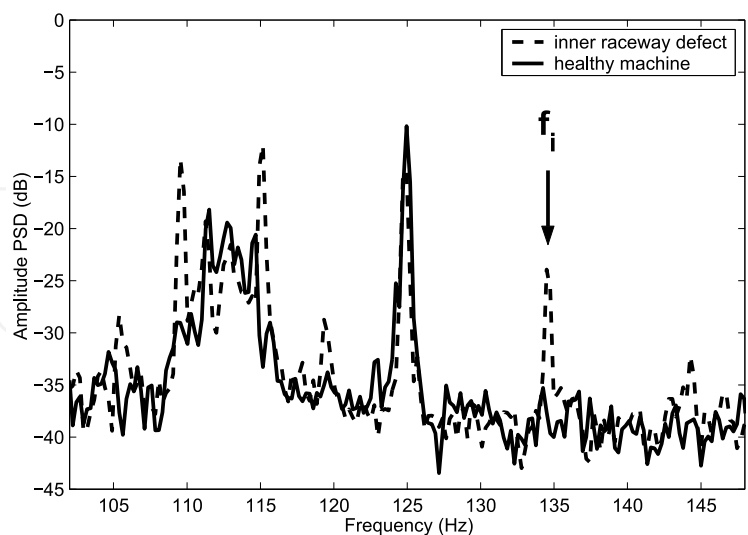
Fig. 26. Torque spectrum of unloaded machine with inner raceway defect.

The stator current spectrum (see Fig. 27) shows, on the one hand, a rise of eccentricity related components. The frequency components at $5f_s + f_r$ and $7f_s - f_r$ are already present in the spectrum of the healthy machine due to an inherent level of dynamic eccentricity. The fault
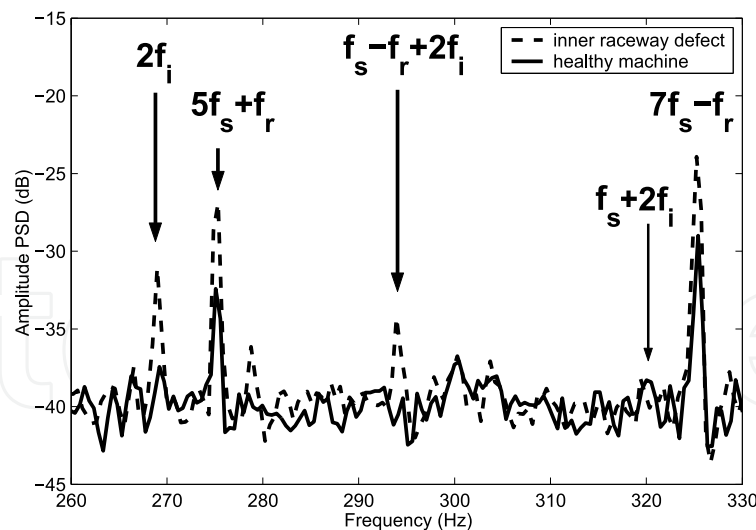
Fig. 27. Stator current spectrum of unloaded machine with inner raceway defect.

related eccentricity increases these components according to (62) (with k=0). The component at $f_s - f_r + 2f_i$ does not appear in the healthy spectrum but in case of the fault as it is the consequence of the particular form of eccentricity introduced by the inner raceway fault. Another fault related component at $2f_i$ can be noticed. The obtained results for this fault validate therefore the precedent theoretical development.

6.6.4 Realistic bearing fault

After artificially produced single point bearing defects, tests were conducted with industrially used bearings that have been changed due to a problem with an unknown fault type. The tested bearing shows only small effects on the vibration spectrum such as a small peak at 33 Hz and a slight general increase of the vibration level for frequencies higher than 150 Hz. Characteristic vibration frequencies could not have been clearly identified.

However, the measured machine torque shows considerable changes in comparison to the healthy case (see Fig. 28). At nominal load level, torque oscillations of great amplitude can be identified at 33 Hz and its multiples.

These torque variations have a considerable effect on the stator current. In Fig. 29, the stator current spectrum with the faulty bearing can be compared to the healthy machine. Sideband components to the fundamental appear at $50 \pm k \cdot 33$ Hz. This is the characteristic signature on the spectrum of a phase modulation of the fundamental component (see (24)).

In order to analyze the phase modulation, the stator current IF is computed. In Fig. 30, the power spectral density (PSD) of the stator current IF is shown for the healthy and faulty case. The significant difference is a component at 33 Hz in the faulty case. The spectral peak at this frequency indicates IF oscillations at 33 Hz. These IF oscillations are a sign of phase modulations present in the faulty case. Considering the measured torque oscillations with the faulty bearing (see Fig. 28), it can be concluded that the observed phase modulation is the consequence of the recognized torque oscillations as it has been developed in section 2.1.

6.6.5 Summary of Experimental Results

The previous experimental results have validated several theoretical aspects. The produced single point defects showed the expected effects on the vibration spectrum i.e. the apparition
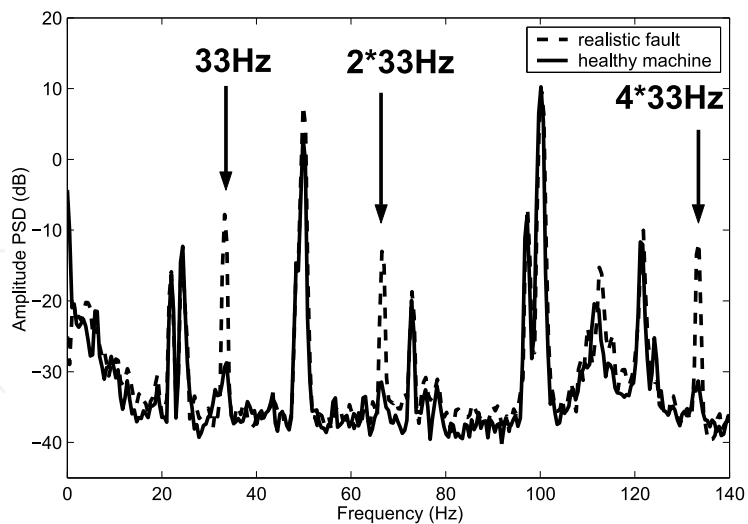
Fig. 28. Torque spectrum of loaded machine with realistic bearing fault.
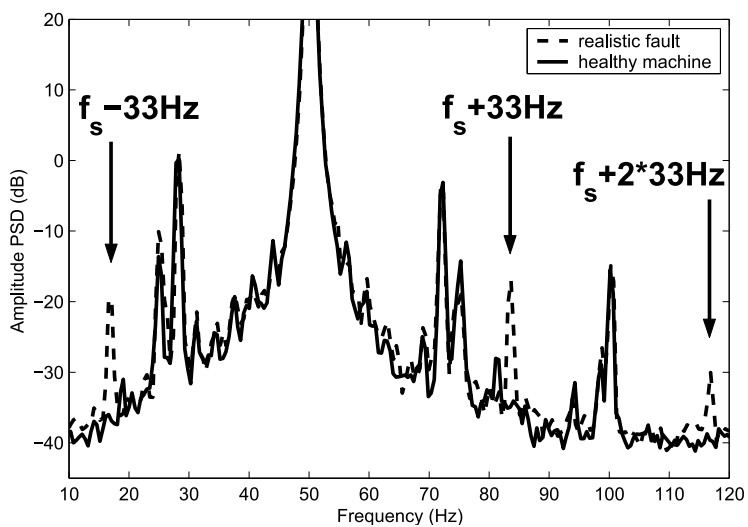

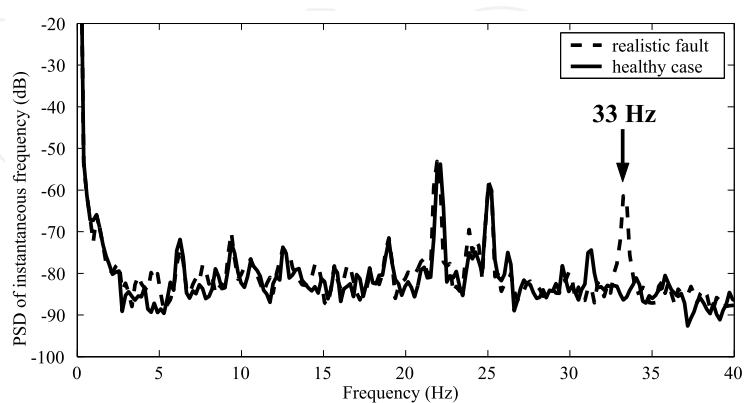Fig. 29. Stator current spectrum of loaded machine with realistic bearing fault.

Fig. 30. Spectrum of stator current instantaneous frequency, loaded machine with realistic
bearing fault.

of the characteristic vibration frequencies. In case of inner and outer race faults, the measured load torque showed oscillations at these frequencies confirming that the assumption of bearing fault-related torque oscillations is valid. Furthermore, significant effects could be observed in the stator current spectrum i.e. the apparition of some of the theoretically predicted frequencies.

Moreover, low frequency load torque oscillations have been observed with a realistic bearing fault. The resulting stator current shows phase modulations which validates the second part of the theoretical study.

However, it must be noted that the amplitudes of the additional stator current frequencies may depend heavily on the considered bearing and the load condition. Therefore, a systematic bearing monitoring using only the stator current is difficult to realize. Nevertheless, in some cases, the stator current showed more significant effects than the vibration data which suggests that a combined approach using vibration and current analysis could be reasonable.

7. Conclusion

This work has investigated mechanical fault detection in induction motors by stator current monitoring. Through a theoretical approach, stator current models were derived that contain different modulations, AM and PM, caused by eccentricity and torque oscillations. Three signal processing methods suitable for stator current analysis and fault detection were described: classical spectrum analysis, suitable only for stationary signals, instantaneous frequency analysis and the Wigner distributions as time-frequency analysis methods that can also be applied with varying supply frequency as can be found with variable-speed drives. It was also demonstrated that the Wigner distribution is a tool for distinguishing eccentricity related faults from faults causing load torque oscillation.

The theoretically derived fault signatures are then validated in experimental setups: first, dynamic eccentricity and load torque oscillations are investigated under laboratory conditions. Then, the detection of misalignment faults in electric winches was presented as an example in a realistic drive system.

As a particular class of faults, bearing faults were also considered. A theoretical development has shown that these faults lead to particular forms of eccentricity and load torque oscillations. After deriving the fault frequencies and modulation types, faulty bearing were examined under laboratory conditions. The obtained results are examples that bearing faults can lead to detectable changes in the stator current.

It can be concluded, that stator current monitoring is a suitable tool for mechanical fault detection in electrical drives. Stator current analysis is certainly more complex than traditional vibration signal analysis due to the fact that the vibration signals are physically closer to the fault. However, it offers advantages over vibration analysis in terms of cost and possibilities of application.

8. References

A. Reilly, G. F. & Boashash, B. (1994). *IEEE Trans. on Signal Processing* **42**(11): 3241–3245.

Albrecht, P. F., Appiairius, J. C., Cornell, E. P., Houghtaling, D. W., McCoy, R. M., Owen, E. L. & Sharma, D. K. (1987). Assessment of the reliability of motors in utility applications - part 1, **EC-2**(3): 396–406.

Auger, F., Flandrin, P., Gonçalvès, P. & Lemoine, O. (1995/1996). Time-frequency toolbox, CNRS / Rice University, France.

URL: *http://tftb.nongnu.org*

Blödt, M. (2006). *Condition Monitoring of Mechanical Faults in Variable Speed Induction Motor Drives - Application of Stator Current Time-Frequency Analysis and Parameter Estimation (available online)*, PhD thesis, Institut National Polytechnique de Toulouse, Toulouse, France.

Blödt, M., Bonacci, D., Regnier, J., Chabert, M. & Faucher, J. (2008). On-line monitoring of mechanical faults in variable-speed induction motor drives using the wigner distribution, *IEEE Transactions on Industrial Electronics* **55**(2).

Blödt, M., Chabert, M., Regnier, J. & Faucher, J. (2006). Mechanical load fault detection in induction motors by stator current time-frequency analysis, *IEEE Transactions on Industry Applications* **42**(6): 1454 – 1463.

Blödt, M., Chabert, M., Regnier, J., Faucher, J. & Dagues, B. (2005). Detection of mechanical load faults in induction motors at variable speed using stator current time-frequency analysis, *Proc. IEEE International Symposium on Diagnostics for Electric Machines, Power Electronics and Drives (SDEMPED '05)*, Vienna, Austria.

Blödt, M., Granjon, P., Raison, B. & Rostaing, G. (2008). Models for bearing damage detection in induction motors using stator current monitoring, *IEEE Transactions on Industrial Electronics* **55**(4): 1813 – 1822.

Blödt, M., Regnier, J. & Faucher, J. (2006). Distinguishing load torque oscillations and eccentricity faults in induction motors using stator current wigner distribution, *Proc. IEEE Industry Applications Society Annual Meeting 2006*, Tampa, Florida.

Boashash, B. (2003). *Time Frequency Signal Analysis and Processing - A Comprehensive Reference*, first edn, Elsevier, Oxford, UK.

Bonaldi, E. L., da Silva, L. E. B., Lambert-Torres, G., Oliveira, L. E. L. & Assuncao, F. O. (2002). Using rough sets techniques as a fault diagnosis classifier for induction motors, *Proc. IEEE IECON'02*, Vol. 4, Sevilla, Spain, pp. 3383–3388.

Cameron, J. R. & Thomson, W. T. (1986). Vibration and current monitoring for detecting airgap eccentricities in large induction motors, *IEE Proceedings* **133**(3): 155–163.

Dorrell, D. G. (1996). Calculation of unbalanced magnetic pull in small cage induction motors with skewed rotors and dynamic rotor eccentricity, *IEEE Transactions on Energy Conversion* **11**(3): 483–488.

Dorrell, D. G., Thomson, W. T. & Roach, S. (1997). Analysis of airgap flux, current, and vibration signals as a function of the combination of static and dynamic airgap eccentricity in 3-phase induction motors, *IEEE Transactions on Industry Applications* **33**(1): 24–34.

Engelmann, R. H. & Middendorf, W. H. (1995). *Handbook of Electric Motors*, Marcel Dekker, New York.

Eren, L., Karahoca, A. & Devaney, M. J. (2004). Neural network based motor bearing fault detection, *Proc. Instrumentation and Measurement Technology Conference (IMTC '04)*, Vol. 3, Como, Italy, pp. 1657–1660.

Flandrin, P. (1999). *Time-Frequency/Time-Scale Analysis*, Academic Press, San Diego.

Goodwin, M. J. (1989). *Dynamics of rotor-bearing systems*, Unwin Hyman, London.

Heller, B. & Hamata, V. (1977). *Harmonic Field Effects in Induction Machines*, Elsevier, Amsterdam, Netherlands.

IEEE motor reliability working group (1985a). Report on large motor reliability survey of industrial and commercial installations, **IA-21**(4): 853–872.

IEEE Motor reliability working group (1985b). Report on large motor reliability survey of industrial and commercial installations, **IA-21**(4): 853–872.

Kay, S. M. (1988). *Modern Spectral Estimation: Theory and Application*, Prentice Hall, Englewood Cliffs, New Jersey.

Li, B., Chow, M., Tipsuwan, Y. & Hung, J. (2000). Neural-network based motor rolling bearing fault diagnosis, 47(5): 1060–1069.

MacFadden, P. D. & Smith, J. D. (1984). Model for the vibration produced by a single point defect in a rolling element bearing, *Journal of Sound and Vibration* **96**(1): 69–82.

Max, J. & Lacoume, J.-L. (2000). *Méthodes et techniques de traitement du signal*, 5th edn, Dunod, Paris.

Mecklenbräuker, W. & Hlawatsch, F. (eds) (1997). *The Wigner Distribution — Theory and Applications in Signal Processing*, Elsevier, Amsterdam (The Netherlands).

Schiltz, R. L. (1990). Forcing frequency identification of rolling element bearings, *Sound and Vibration* pp. 16–19.

Schoen, R. R., Habetler, T. G., Kamran, F. & Bartheld, R. (1995). Motor bearing damage detection using stator current monitoring, *IEEE Transactions on Industry Applications* **31**(6): 1274–1279.

Sekhar, A. S. & Prabhu, B. S. (1995). Effects of coupling misalignment on vibrations of rotating machinery, *Journal of Sound and Vibrations* **185**(4): 655–671.

Sieg-Zieba, S. & Tructin, E. (2008). Handling systems condition monitoring using vibrations and motor current, *Proc. Condition Monitoring*, Edinburgh, Scotland.

Stack, J., Habetler, T. G. & Harley, R. G. (2004a). Bearing fault detection via autoregressive stator current modeling, *IEEE Transactions on Industry Applications* **40**(3): 740–747.

Stack, J., Habetler, T. G. & Harley, R. G. (2004b). Fault classification and fault signature production for rolling element bearings in electric machines, *IEEE Transactions on Industry Applications* **40**(3): 735–739.

Tandon, N. & Choudhury, A. (1997). An analytical model for the prediction of the vibration response of rolling element bearings due to a localized defect, *Journal of Sound and Vibration* **205**(3): 275–292.

Teotrakool, K., Devaney, M. J. & Eren, L. (2006). Adjustable speed drive bearing fault detection via wavelet packet decomposition, *Proc. Instrumentation and Measurement Technology Conference (IMTC '06)*, Sorrento, Italy, pp. 22–25.

Timár, P. L. (1989). *Noise and Vibration of Electrical Machines*, Elsevier, North-Holland.

Wang, Y. F. & Kootsookos, P. J. (1998). Modeling of low shaft speed bearing faults for condition monitoring, *Mechanical Systems and Signal Processing* **12**(3): 415–426.

Xu, M. & Marangoni, R. D. (1994a). Vibration analysis of a motor-flexible coupling-rotor system subject to misalignment and unbalance, part i: theoretical model and analysis, *Journal of Sound and Vibrations* **176**(5): 663–679.

Xu, M. & Marangoni, R. D. (1994b). Vibration analysis of a motor-flexible coupling-rotor system subject to misalignment and unbalance, part ii: experimental validation, *Journal of Sound and Vibrations* **176**(5): 681–691.

Yang, S. J. (1981). *Low-noise electrical motors*, Clarendon Press, Oxford.

Zhou, W., Habetler, T. G. & Harley, R. G. (2007). Stator current-based bearing fault detection techniques: A general review, *IEEE International Symposium on Diagnostics for Electric Machines, Power Electronics and Drives (SDEMPED)*, Cracow, Poland, pp. 7–10.

Zhou, W., Habetler, T. G. & Harley, R. G. (2008). Bearing fault detection via stator current
       noise cancellation and statistical control, *IEEE Transactions on Industrial Electronics*
       55(12): 4260–4269.

Fault Detection

Edited by Wei Zhang

In this book, a number of innovative fault diagnosis algorithms in recently years are introduced. These methods can detect failures of various types of system effectively, and with a relatively high significance.

How to reference

In order to correctly reference this scholarly work, feel free to copy and paste the following:

Martin Blodt, Pierre Granjon, Bertrand Raison and Jeremi Regnier (2010). Mechanical Fault Detection in Induction Motor Drives through Stator Current Monitoring - Theory and Application Examples, Fault Detection, Wei Zhang (Ed.), ISBN: 978-953-307-037-7, InTech, Available from: http://www.intechopen.com/books/fault-detection/mechanical-fault-detection-in-induction-motor-drives-through-stator-current-monitoring-theory-and-ap

INTECH
open science | open minds